

Role of Indian Ocean basin mode in driving the interdecadal variations of summer precipitation over the East Asian monsoon boundary zone

Jing Wang^{1,*}, Yanju Liu², Fei Cheng^{3,*}, Chengyu Song⁴, Qiaoping Li⁵, Yihui Ding², Xiangde Xu⁶

¹Tianjin Key Laboratory for Oceanic Meteorology, and Tianjin Institute of Meteorological Science, Tianjin, China

²National Climate Center, China Meteorological Administration, Beijing, China

³Ningbo Meteorological Observatory, Ningbo, China

⁴Heilongjiang Climate Centre, Harbin, China

⁵CMA Earth System Modelling and Prediction Centre, Beijing, China

⁶State Key Laboratory of Severe Weather, Chinese Academy of Meteorological Sciences, Beijing, China

Correspondence: Yanju Liu (liuyan@cmac.gov.cn)

* Jing Wang and Fei Cheng contributed equally to this work.

Abstract. Based on long-term observational and reanalysis datasets from 1901 through 2014, this study investigates the characteristics and physical causes of the interdecadal variations in the summer precipitation over the East Asian monsoon boundary zone (EAMBZ). Observational evidence reveals that the EAMBZ precipitation featured prominent interdecadal fluctuations, e.g., with dry summers during the periods preceding 1927, 1939–1945, 1968–1982, and 1998–2010, and wet summers during the periods of 1928–1938, 1946–1967, and 2011 onwards. Further analyses identify that the Indian Ocean basin mode (IOBM) is an important oceanic modulator responsible for the interdecadal variations of the EAMBZ precipitation. When the cold phase of the IOBM occurs, an anomalous cyclonic circulation is excited around the northeast corner of the tropical Indian Ocean, which further induces a “north-low–south-high” meridional seesaw pattern over the Northeast China–subtropical western Pacific (SWP) sector. Such seesaw pattern is conducive to the enhanced EAMBZ precipitation through linking favorable environments for the transportation of water vapor from the SWP and the convergence over EAMBZ at interdecadal timescales. For this reason, a physical-empirical model for the EAMBZ precipitation is developed in terms of the IOBM cooling, which can well capture its interdecadal fluctuations and reflect their steady relationship. The key physical pathway connecting the IOBM cooling with the interdecadal variations of the summer EAMBZ precipitation is supported by the numerical results based on the large ensemble experiment and the Indian Ocean pacemaker experiment. Our findings may provide new insights into the understanding of the causes of the interdecadal variations in the summer EAMBZ precipitation, which may favor the long-term policy decision making for the local hydrometeorological planning.

1 Introduction

The monsoonal airflows and mid-latitude westerlies are crucial components of the Asian climate system (Li and Zeng, 2002; Ding and Chan, 2005; Wang et al., 2008; Wu et al., 2012; Huang et al., 2015; Wang et al., 2017; Chen et al., 2018; J. Huang et al., 2019). These two subsystems can synergistically induce regional precipitation fluctuations over subtropical and mid-latitude Asia during the Northern Hemisphere (NH)–late spring (May) and summer (June–July–August; JJA) (Qian et al., 2009; Chen et al., 2021; Song et al., 2022; J. Wang et al., 2022). For example, Song et al. (2022) found that May precipitation over the southeastern extension of the Tibetan Plateau (TP) features notable year-to-year variations, which are physically linked to a unique interplay between the upstream mid-latitude westerlies and the Bay of Bengal summer monsoon.

44

45 During the early stage of the northern summer, however, the mid-latitude ~~NH~~-westerlies shift poleward to the north of
46 the TP abruptly (Yeh et al., 1959; Schiemann et al., 2009). In this context, westerlies of mid-latitude synoptic disturbance
47 and southerlies of East Asian summer monsoon (EASM) collide with each other frequently over the East Asian monsoon
48 boundary zone (EAMBZ) (Qian et al., 2009; Wang et al., 2017; Chen et al., 2018; J. Huang et al., 2019; Zeng and Zhang,
49 2019; Chen et al., 2021; Q. Wang et al., 2021, 2022, 2023). EAMBZ is a transitional climate zone between the EASM-
50 controlled moist region and the westerly-dominated arid region over central Asia (Chen et al., 2010; Chen et al., 2018,
51 2021), stretching from the eastern flank of the TP to Mongolia and Northeast China [see Fig. 1 in Chen et al. (2021)]; also
52 see the red box in Fig. 1]. Notably, EAMBZ is a distinguished region with agrarian economy and animal husbandry, which
53 is largely susceptible to water resource variations (Ou and Qian, 2006; Lu and Jia, 2013). Nevertheless, many studies
54 reported that in the past century, the semi-arid EAMBZ underwent the most profound warming over East Asia, suffering
55 from serious aridification and a high risk of desertification (J. Huang et al., 2017, 2019, 2020). In this regard, EAMBZ is
56 deemed one of the “hotspots” highly sensitive to precipitation fluctuations (Qian et al., 2009; Lu and Jia, 2013; J. Huang
57 et al., 2019). Given that the EAMBZ is of an ecologically fragile environment with water shortage, a deep understanding
58 of the reasons for historical changes in summer EAMBZ precipitation could be a prerequisite for in situ ecological
59 improvement and socioeconomic development.

60

61 Existing studies have well documented physical mechanisms responsible for the interannual variability of summer
62 EAMBZ precipitation, highlighting the external moisture supply pathways, the modulators for the wet-dry condition
63 variations [e.g., the mid-latitude westerlies within the Asian westerly jet (~~AWJ~~), the western North Pacific (~~WNP~~)
64 subtropical high (~~WNPSH~~), and the EASM], and the remote modulation roles of large-scale teleconnected modes [e.g.,
65 Silk Road pattern (~~SRP~~)/circumglobal teleconnection (~~CGT~~) propagating along the westerly jet AWJ and the Eurasian
66 teleconnection (~~EU~~)] and sea surface temperature (SST) anomaly patterns (Huang et al., 2015; Wang et al., 2017; Chen
67 et al., 2018, 2021; Zhao et al., 2019a, 2019b, 2020; Q. Wang et al., 2021, 2022, 2023). For instance, Q. Wang et al. (2022)
68 suggested that the positive phase of the Eurasian teleconnection EU-phase is connected with a low pressure anomaly in
69 the lower troposphere in EAMBZ and the Mongolia region, thus favoring enhanced summertime precipitation over
70 EAMBZ; and meanwhile, the circumglobal teleconnection CGT is positively coupled with the EAMBZ precipitation, with
71 ascending motion anomalies over EAMBZ during its positive phase. Chen et al. (2021) established that the circulations
72 (i.e., the mid-latitude westerlies and EASM) and the forcing of SST anomalies (SSTAs) can collectively regulate the
73 summer EAMBZ precipitation variability. The variability of westerlies is largely modulated by the Silk Road pattern SRP
74 and the meridional displacement of the westerly jet AWJ; while the EASM variability is mainly modulated by the prior
75 wintertime El Niño-Southern Oscillation (~~ENSO~~). The synchronized effects of EASM and westerlies largely contribute
76 to the rainfall variability in EAMBZ. Note that Chen et al. (2021) also pointed out that the Indian Ocean basin mode
77 (IOBM) is simultaneously correlated with the EASM in boreal summer on the interannual timescale, which may be
78 considered as a salient oceanic modulator for the summer EAMBZ precipitation variability. Nevertheless, they paid little
79 attention to the physical mechanisms of how IOBM regulates the year-to-year EAMBZ precipitation. Moreover, Zhao et
80 al. (2019a) found that the tropical northern Atlantic SSTAs have significant impacts on the August rainfall over the
81 monsoon transitional zone in China through inducing a wavetrain over Eurasia and ~~an anomalous WNPSH~~the western
82 North Pacific anomalous anticyclone.

83

84 Compared with the extensively explored interannual variability of the JJA EAMBZ precipitation, less efforts have been
85 devoted to its interdecadal variability. To understand and predict the summer EAMBZ precipitation, exploring its
86 interdecadal variations and the underlying physical causes are also critical, which are the main focus of the present study.

87 Previous studies suggested that the warm-season precipitation over many Asian areas features interdecadal fluctuations.
88 For example, J. Wang et al. (2022) reported that the late spring (May) southeastern TP underwent wet conditions for
89 1928–1961 and 1989–2003, and experienced dry conditions preceding 1927, 1962–1988, and 2004 onwards. Si and Ding
90 (2016) documented that East Asia experienced dry summers from the early 1920s to the 1940s, as well as wet summers
91 from the late 1900s to the early 1920s, in the 1950s, and from the 1980s to the 1990s. Piao et al. (2021) found that the
92 decadal-filtered summer precipitation over Northeast Asia underwent a sudden decrease around the late 1990s. The oceanic
93 interdecadal signals for these interdecadal changes are also extensively investigated, highlighting the crucial modulation
94 roles of basin-scale SST modes of Atlantic multidecadal oscillation—(~~AMO~~), Pacific decadal oscillation
95 (~~PDO~~)/interdecadal Pacific oscillation (IPO), and IOBM (Si et al., 2021). Among these interdecadal oceanic forcings, it
96 is essential to emphasize the IOBM, a dominant mode of SST variability in the tropical Indian Ocean (TIO) sector, which
97 usually follows up a wintertime El Niño-Southern Oscillation~~ENSO~~ event and persists into the summer through the
98 capacitor effect (Klein et al., 1999; Yang et al., 2007; Xie et al., 2009). It is worth noting that the IOBM also features a
99 basin-scale warming/cooling at interdecadal timescales (Han et al., 2014), exerting active impacts on the mid-latitude
100 Asian climate (e.g., Wu et al., 2016; Li and Ma, 2018; Zhang et al., 2018; S. Wang et al., 2022). As for the interdecadal
101 variations of the summer EAMBZ precipitation, we hope to answer the following two questions: 1) Did the JJA EAMBZ
102 precipitation feature interdecadal variations? If so, 2) is there any intimate connection between IOBM and the EAMBZ
103 precipitation at interdecadal timescales? As such, this study shall extend previous studies by exploring what extent and
104 how the JJA IOBM modulate the concurrent EAMBZ precipitation variability at interdecadal timescales, with the aim of
105 providing a novel understanding for the rainfall variability over the mid-latitude semi-arid zone in Asia. Note that we
106 employ datasets with a centennial scale in this study [e.g., the precipitation data produced by the Climatic Research Unit
107 (CRU) and the atmospheric circulation data from the Twentieth Century Reanalysis (~~20CR~~) datasets]. In comparison with
108 the short-term datasets since the latter half of the 20th century, these long-term datasets can separate the interdecadal
109 variability of EAMBZ precipitation from the externally forced global climate change caused by anthropogenic (e.g.,
110 greenhouse gas) and natural forcings (e.g., volcanic eruption) more effectively (Wu et al., 2016), which were widely used
111 to investigate the physical causes of how internal fluctuations of the climate system modulate the interdecadal variations
112 of precipitation over Asia (e.g., Wu et al., 2016; Zhang et al., 2018; Sun et al., 2019a; Jiang et al., 2021; J. Wang et al.,
113 2022).

114
115 The remainder of this paper is arranged as follows. Section 2 describes the datasets and methods used in this study. Section
116 3 elucidates the characteristics of the interdecadal variations of summertime EAMBZ precipitation and the associated
117 background circulations, illustrates the mechanisms of how IOBM modulates the EAMBZ precipitation, establishes a
118 linear regression model using the IOBM to predict the interdecadal precipitation anomalies over EAMBZ, and verifies
119 the IOBM-related physical processes using numerical model simulations. A summary of the major findings and further
120 discussions are provided in Section 4.

122 **2 Datasets and methods**

124 **2.1 Observational Data**

125
126 Several monthly mean observational datasets are utilized in the present study, including (1) the global land high-resolution
127 gridded CRU time series (~~TS~~)-precipitation dataset version 3.26 (CRU TS3.26; spatial resolution: $0.5^\circ \times 0.5^\circ$; Harris et al.,
128 2014) for 1901–2017, (2) the Extended Reconstructed SST version 5 (ERSSTv5; spatial resolution: $2^\circ \times 2^\circ$; B. Huang et
129 al., 2017) for 1854–present derived from the National Oceanic and Atmospheric Administration (NOAA), and (3)

130 atmospheric variables derived from NOAA–Cooperative Institute for Research in Environmental Sciences (CIRES)
 131 [Twentieth Century Reanalysis20CR](#) version 2c (20CRv2c; spatial resolution: 2°×2°; [Compo et al., 2011](#)), except for the
 132 precipitation data, with 192 points in longitude and 94 points in latitude, for 1851–2014. Note that all observational
 133 datasets cover the common time period of 1901–2014, which is the focused period in the present research.

134

135 **2.2 Rossby wave source**

136

137 Following [Sardeshmukh and Hoskins \(1988\)](#), the Rossby wave source (RWS) is calculated as:

$$138 \quad RWS = -\nabla \cdot [V_{\chi}(\zeta + f)], \quad (1)$$

139 where V_{χ} is the divergent wind, ζ is the relative vorticity, and f is the planetary vorticity.

140

141 **2.3 Moisture flux and associated divergence**

142

143 The vertically integrated horizontal water vapor transport ($\langle WVT \rangle$) and WVT-associated divergence ($\langle WVT_div \rangle$) are
 144 calculated using the following equations ([Sun et al., 2019b](#); [J. Wang et al., 2022](#)):

$$145 \quad \langle WVT \rangle = -\frac{1}{g} \int_{P_s}^{300} q \vec{V} dp, \quad (2)$$

$$146 \quad \langle WVT_div \rangle = -\frac{1}{g} \int_{P_s}^{300} \nabla_p \cdot (q \vec{V}) dp, \quad (3)$$

147 where $\nabla_p \cdot ()$ denotes the horizontal divergence in the pressure coordinates; g is the gravitational acceleration; P_s is the
 148 surface pressure; q is the specific humidity; and $\vec{V} = (u, v)$ is the horizontal wind vector (u and v represent the zonal and
 149 meridional winds, respectively).

150

151 **2.4 Statistical methods**

152

153 This study focuses on interdecadal fluctuations in variables. The data are 11-year low-pass filtered by adopting a Lanczos
 154 filter ([Duchon, 1979](#)) to extract the corresponding interdecadal signal. Several statistical methods are used, including
 155 empirical orthogonal function (EOF) analysis, composite analysis, correlation analysis, and linear regression analysis. A
 156 two-tailed Student's t test is used to evaluate the statistical significance. Considering the 11-year low-pass filtered method
 157 can significantly reduce the degrees of freedom of the data, the following approximation is therefore deployed to calculate
 158 the effective degrees of freedom (N^{eff}):

$$159 \quad \frac{1}{N^{eff}} \approx \frac{1}{N} + \frac{2}{N} \sum_{j=1}^N \frac{N-j}{N} \rho_{XX}(j) \rho_{YY}(j), \quad (4)$$

160 where N is the sample size, and $\rho_{XX}(j)$ and $\rho_{YY}(j)$ are the autocorrelations of two sampled time series X and Y ,
 161 respectively, at time lag j ([Li et al., 2013](#)).

162

163 In this study, we focus on the boreal summer season (JJA). All variables in observations and model simulations are
 164 linearly detrended before further calculations and analyses to exclude potential impacts of long-term trends.

165

166 2.5 Definitions

167

168 2.5.1 The research domain of EAMBZ

169

170 From the long-term (1901–2014) perspective of the climatological mean state of converged <WVT> and pronounced
171 precipitation over the mid-latitude Asia, the EAMBZ (box in **Figs. 1a** and **1b**; 35°–55°N, 105°–130°E) is defined as the
172 collision and convergence zone between JJA dry westerly <WVT> and moist southwesterly <WVT> (**Fig. 1a**). As such,
173 there exist wetter conditions over the EASM-dominated part and drier conditions over the westerly-controlled part (**Fig.**
174 **1b**), suggesting the semi-arid transitional feature of EAMBZ (Xing and Wang, 2017). Our defined research domain of
175 EAMBZ largely matches the monsoon boundary zone defined by Chen et al. (2021), covering Inner Mongolia, Gansu,
176 Ningxia, Shaanxi, Shanxi, Hebei, Beijing, Tianjin, Shandong, Jilin, Liaoning, and Heilongjiang in China, as well as
177 eastern Mongolia and Korean peninsula. Note that the areal mean precipitation over EAMBZ in boreal summer is the
178 highest of the year accompanying the largest standard deviation (i.e., largest rainfall variability) (**Fig. S1**), which is the
179 focused season in the present study.

180

181 2.5.2 Climate indices

182

183 The IOBM index (I_{IOBM}) is defined as areal mean SSTAs over the TIO domain of 20°S–20°N, 40°–100°E (Xie et al.,
184 2009). The IPO index is calculated using a method identical to that defined in Henley et al. (2015), that is, the difference
185 between SSTAs averaged over the central equatorial Pacific (10°S–10°N, 170°E–90°W) and the average of SSTAs in the
186 northwest (25°–45°N, 140°E–145°W) and the southwest Pacific (50°S–15°S, 150°E–160°W). In observations,
187 considering the coupled nature of IOBM and IPO at interdecadal timescales in boreal summer [cf. Fig. 2a in Wu et al.
188 (2016)], we hence remove the potential influence of the contemporaneous IPO on precipitation via eliminating the signal
189 of IPO index from the data of climate variables based on the partial regression technique, which is widely used in previous
190 studies (e.g., Dou and Wu, 2018; J. Wang et al., 2022).

191

192 2.6 Model simulations

193

194 To validate our proposed mechanisms of how the TIO SSTAs (i.e., IOBM-associated SSTAs) remotely modulate the
195 summer EAMBZ precipitation on interdecadal timescales, following the method of Zhang et al. (2019) and Yang et al.
196 (2020), we adopt monthly mean outputs from two experiments of the Community Earth System Model version 1 (CESM1),
197 which is a fully coupled Earth system model incorporating components of atmosphere, ocean, land, and sea ice (Hurrell
198 et al., 2013).

199

200 The first experiment is the CESM1 Large Ensemble Numerical Simulation (referred to as CESM1_LENS; Kay et al.,
201 2015). Among total 40 ensemble members in CESM1_LENS (Yang et al., 2020), we use the first 35 individual members
202 according to many previous studies (e.g., Touma et al., 2021; J. Wang et al., 2023), which were completed at the climate
203 modeling center of National Center for Atmospheric Research (NCAR). Note that all ensemble members in
204 CESM1_LENS were imposed with the same radiative forcing scenario (Taylor et al., 2012), with historical forcing for
205 1920–2005 and high-emission forcing scenario (i.e., Representative Concentration Pathway (RCP) 8.5) for 2006–2080
206 (Moss et al., 2010; Touma et al., 2021). The ensemble members were further generated with slightly differentiated
207 perturbations of atmospheric states (Kay et al., 2015; Touma et al., 2021). The second experiment is the CESM1 Indian
208 Ocean Pacemaker Ensemble Simulation (referred to as CESM1_IOPES), with 10 ensemble members (Zhang et al., 2019;

209 Yang et al., 2020). We adopt CESM1_IOPES to highlight the impact of SSTAs over the broader TIO domain (15°S–15°N,
210 African coast to 174°E). For the convenience of subsequent calculations and analyses, the African coast is designated as
211 40°E in this study, and a small change in the longitudes regarding the African coast may not affect the main results.

212
213 As indicated by Yang et al. (2020), the CESM1_LENS 35-member ensemble mean results can better provide an estimate
214 of the influence of the external radiative forcing signals (e.g., greenhouse gas) on the climate system. Furthermore, the
215 10-member ensemble mean results in CESM1_IOPES contain the responses to both external forcings and the observed
216 SST variations over the TIO domain (Yang et al., 2020). Therefore, by subtracting the CESM1_LENS ensemble mean
217 from the CESM1_IOPES ensemble mean, we can obtain responses of the climate system to the internal variability
218 stemming from the time-varying TIO SSTAs, distinguishing the impact of external radiative force changes from the
219 intrinsic variability driven by TIO SSTAs. More details about CESM1_LENS and CESM1_IOPES can be found in Kay
220 et al. (2015) and Yang et al. (2020), respectively. The variables employed here comprise precipitation and wind in
221 atmosphere component of Community Atmospheric Model version 5-(CAM5), with a spatial resolution of 1.25° in
222 longitude and 0.9° in latitude; and SST in the ocean component of Parallel Ocean Program version 2-(POP), with 320
223 grids in longitude and 384 grids in latitude. Before further analyses, model outputs are interpolated at a resolution of 2°×2°
224 using a bilinear interpolation method (Mastyło, 2013), identical to that of 20CRv2c. In the current study, we focus on the
225 historical simulation period of 1920–2005.

226
227 Here, it is important to stress the following two points. First, although the TIO domain in CESM1_IOPES is broader than
228 that for defining I_{IOBM} , there exist highly consistent temporal variations in SSTAs between them in observations (Fig. S2)
229 and simulations (Fig. S3) at interdecadal timescales, with temporal correlation coefficients (TCCs) of 0.93 and 0.87 ($P <$
230 0.01), respectively. Second, when selecting the SSTAs over the broader TIO domain (purple box in Fig. S4) as a metric,
231 it can be found that the observed (Fig. S4a) and modelled (Fig. S4b) large and intense loadings of the positive SSTAs are
232 still concentrated around the narrower TIO domain (black box in Fig. S4). As such, it is plausible to adopt the above-
233 mentioned Indian Ocean pacemaker experiment with broader TIO SSTAs to validate our proposed mechanisms tied to
234 the interdecadal IOBM variations.

235

236 3 Results

237

238 3.1 Observed interdecadal variations of the summer precipitation over EAMBZ and related 239 background circulations

240

241 **Figure 1c** plots the spatial distribution of the interdecadal standard deviation of precipitation. This distribution is quite
242 similar to that of the climatology (Fig. 1b), suggesting relatively strong (weak) interdecadal precipitation fluctuations
243 over the EASM-dominated (westerly-controlled) part of the EAMBZ. Moreover, we show the first EOF mode of JJA-
244 mean EAMBZ precipitation (Fig. 1d), which accounts for 28% of the total variance and distinguishes from the remaining
245 eigenvectors according to the criterion defined by North et al. (1982). The leading EOF mode bears close resemblance to
246 the standard deviation of the EAMBZ precipitation on interdecadal timescales (Figs. 1c and 1d), with larger loadings
247 occupying the Bohai Sea and Korean peninsula and their adjoining regions. The interdecadal TCC between the principal
248 component of the EOF1 and area-averaged precipitation over the research domain of EAMBZ (35°–55°N, 105°–130°E)
249 [EAMBZ precipitation index (I_{EAMBZP} for short); Fig. 1e] is 0.93 ($P < 0.001$). The aforementioned results indicate that
250 that our defined I_{EAMBZP} can serve as a good indicator of the predominant fluctuations in the precipitation anomalies over
251 EAMBZ at interdecadal timescales. As such, from the time series of 11-year low-passed filtered I_{EAMBZP} (Fig. 1e), we can

252 observe that the summer EAMBZ precipitation delineates notable interdecadal fluctuations. For example, EAMBZ
253 experienced dry summers during the periods preceding 1927, 1939–1945, 1968–1982, and 1998–2010, but underwent
254 wet summers during the periods of 1928–1938, 1946–1967, and 2011 onwards. Note that Si et al. (2021) explored the
255 interdecadal variations of summer precipitation over northeast Asian, a domain that largely matches our focused EAMBZ
256 domain. The observed major interdecadal fluctuation periods of EAMBZ precipitation are basically consistent with those
257 suggested by Si et al. (2021), with dry summers around 1940.

258
259 Before examining the modulation of IOBM on the interdecadal EAMBZ precipitation fluctuations, it is essential to
260 scrutinize the JJA-mean I_{EAMBZP} -associated circulation anomalies. The highest mid-latitude positive correlation region
261 can be discerned north of the TP (38° – 46° N, 80° – 112.5° E; blue box in **Fig. 2a**), suggesting that the interdecadal
262 enhancement of the summer EAMBZ precipitation is intimately correlated with the acceleration of the upstream mid-
263 latitude westerlies at 400 hPa. In light of the method of [Chen et al. \(2021\)](#) and [J. Wang et al. \(2022\)](#), we correlate the
264 I_{EAMBZP} with the zonal winds averaged over the longitudinal range of EAMBZ at multiple levels (**Fig. 2b**) to further check
265 whether the most significant correlation occurs at 400 hPa. Evidently, on interdecadal timescales, the largest positive
266 correlation between precipitation and mid-latitude westerlies within 38° – 46° N does occur at the mid-tropospheric level
267 of 400 hPa, with a TCC of 0.46 ($P < 0.01$) between the I_{EAMBZP} and areal mean 400-hPa zonal winds (U400) over the
268 upstream westerly-dominated domain (**Fig. 2c**). Note that this correlation pattern exhibits a barotropic structure (**Fig. 2b**).
269 Additionally, we correlate the I_{EAMBZP} with the 850-hPa meridional winds (V850). The I_{EAMBZP} is positively correlated
270 with the key monsoonal southerly domain east of the TP (25° – 33° N, 102.5° – 112.5° E; green box in **Fig. 2d**), which is
271 located in the western portion of the EASM domain ([Ying et al., 2023](#)). The interdecadal correlation pattern between
272 meridional winds and the summer EAMBZ precipitation at multiple levels exhibits a baroclinic structure, with the
273 significant positive correlations confined below 500 hPa (**Fig. 2e**). Note that the strongest positive correlation is detected
274 at 850 hPa within 102.5° – 112.5° E, with a TCC of 0.63 (**Fig. 2f**; $P < 0.001$) between I_{EAMBZP} and areal mean 850-hPa
275 meridional winds (V850) over the key EASM-controlled domain (**Fig. 2d**).

276
277 **Figure 3** gives the JJA-mean I_{EAMBZP} -regressed circulation anomalies at interdecadal timescales. The interdecadal
278 enhancement of the EAMBZ precipitation is significantly linked to a localized quasi-barotropic cyclonic (low-pressure)
279 anomaly. At 400 hPa, significant westerly anomalies prevail in its southern flank, inducing the acceleration of westerlies
280 upstream of EAMBZ (**Fig. 3a**). At 850 hPa, the enhanced EAMBZ precipitation is connected to a north-south meridional
281 seesaw pattern, with a significant anticyclonic (high-pressure) anomaly over the subtropical western Pacific (SWP) and a
282 significant cyclonic anomaly over EAMBZ (**Fig. 3b**), exhibiting a somewhat barotropic structure (**Figs. 3a and 3b**).
283 Significant southerly anomalies prevail in the western flank of this SWP clockwise gyre anomaly (SWPCGA). Moreover,
284 from the perspective of $\langle WVT \rangle$ (**Fig. 3c**), the magnitudes of southerly $\langle WVT \rangle$ anomalies over the key EASM-controlled
285 domain tied to the SWPCGA are much greater than the westerly $\langle WVT \rangle$ anomalies over the westerly-dominated domain.
286 Note that the southerly $\langle WVT \rangle$ anomalies are significantly divergent, pushing copious amounts of warm and moist vapor
287 over the SWP into EAMBZ. Then, with the aid of the local anticlockwise $\langle WVT \rangle$ gyre pattern (**Fig. 3c**), the EASM
288 southerlies from the low latitudes, which bring warm temperature advection anomalies, may easily collide with the mid-
289 level cold temperature advection anomalies brought by mid-latitude enhanced westerlies (**Figs. 4a and 4b**), manifesting
290 the extratropical–tropical interplay around EAMBZ on interdecadal timescales. Such interplay is basically aligned with
291 that on interannual timescales (cf. [Chen et al., 2021](#)). Under such environments, atmospheric instability over EAMBZ can
292 be triggered to generate in situ significant ascending motion anomalies responsible for increased precipitation (**Fig. 5a**).
293 Note that considering the greater magnitudes of anomalies of $\langle WVT \rangle$ and warm temperature advection connected to the
294 southerlies over the key EASM-controlled domain, we presume that the monsoonal southerlies play a predominant

295 dynamical role in the interdecadal enhancement of precipitation over EAMBZ. To verify this presumption, we further
296 propose an East Asian monsoon index (I_{MI} for short), defined as the areal mean meridional winds at 850 hPa
297 the key monsoonal southerly domain, and a westerly index (I_{WI} for short), defined as the areal mean 400-hPa zonal
298 winds over the upstream westerly-dominated region. The I_{MI} -regressed results can well and realistically reproduce
299 the magnitudes and distributions of the anomalous upward motions tied to I_{EAMBZP} (**Fig. 5b** vs. **5a**). However, the
300 magnitudes of I_{WI} -regressed results are highly weakened, along with the major loadings shifting more southward (**Fig.**
301 **5c**). Above results could allow us to conclude that the anomalous southerlies over the key monsoonal southerly domain
302 could be the predominant driving factor for the interdecadal enhancement of summer EAMBZ precipitation, whereas the
303 upstream accelerated westerlies play a secondary dynamical amplification role.

304

305 **3.2 Interdecadal relationship between IOBM and the summer EAMBZ precipitation**

306

307 Many previous studies have substantiated that the IOBM can remotely modulate summer rainfall fluctuations over the
308 mid-latitude Asia at interdecadal timescales (e.g., Zhang et al., 2018; S. Wang et al., 2022; Wu et al., 2022). In the present
309 study, we also identify that the IOBM can exert profound impacts on the interdecadal variations of the EAMBZ
310 precipitation in boreal summer. In this subsection, we firstly reveal their intimate relationship. **Figure 6a** exhibits the
311 correlation pattern between the JJA-mean I_{EAMBZP} and the contemporaneous global gridded SST at interdecadal timescales.
312 The most pronounced and significant correlations are found in the TIO sector, which largely matches the domain for
313 delineating the IOBM mode (black frame in **Fig. 6a**). There exists a salient out-of-phase relationship between the
314 interdecadal EAMBZ precipitation changes and the IOBM mode, with a TCC of -0.57 between I_{EAMBZP} and I_{IOBM} (**Fig.**
315 **6b**; $P < 0.01$). This result suggests that IOBM warming (cooling) is significantly connected with dry (wet) EAMBZ
316 summers, which serves as a critical oceanic modulator. On interdecadal timescales, the IOBM can remotely spark
317 conducive dynamical circumstances for increased precipitation over EAMBZ, i.e., the collision between cold and warm
318 airflows around EAMBZ (**Figs. 4c** and **4d**) and the locally significant convergent ascending motion anomalies resembled
319 those tied to the positive I_{EAMBZP} (**Fig. 5d** vs. **5a**). However, the extratropical cold (tropical warm) temperature advection
320 anomalies west (south) of the EAMBZ, which are tied to the strengthened westerlies (southerlies), are quite insignificant
321 (significant) (**Figs. 4c** and **4d**). This indicates that the IOBM may exerts a more profound influence on the southerly wind
322 anomalies over the EASM-controlled domain, which is more important for enhanced EAMBZ precipitation; whereas the
323 IOBM may insignificantly modulate the westerly anomalies over the westerly-dominated region. The possible underlying
324 mechanisms of how IOBM links the summertime circulation anomalies responsible for the interdecadal fluctuations in
325 the EAMBZ precipitation will be illuminated in the next subsection.

326

327 **3.3 Possible mechanisms**

328

329 **Figure 7** shows partial regression of the JJA-mean anomalies of SST and large-scale precipitation over TIO and its
330 neighboring areas onto the I_{IOBM} at interdecadal timescales with the IPO signal removed. Corresponding to higher I_{IOBM}
331 years, warm SSTAs cover almost all areas of TIO, with large loadings appearing in the central-southern TIO and relatively
332 small loadings appearing in the northern TIO (**Fig. 7a**), which are aligned with the previous studies (Wu et al., 2016; Y.
333 Huang et al., 2019). Moreover, there are striking suppressed precipitation around the northeast corner of the TIO domain
334 (**Fig. 7b**), suggesting profoundly localized atmospheric responses (viz. the release of regional anomalous atmospheric
335 cooling) to the warm TIO SSTAs. Note that corresponding to cold TIO SST years, there exist positive precipitation
336 anomalies around the northeast corner of TIO, suggesting the release of anomalous atmospheric heating (figure not
337 shown). Since the significant out-of-phase relationship between summertime IOBM and EAMBZ precipitation at

338 interdecadal timescales, we adopt negative I_{IOBM} -regressed patterns to express the influence of cold SSTAs over the TIO
339 region. **Figure 8** displays the anomalous patterns of the RWS, velocity potential, and divergent horizontal winds regressed
340 onto the negative I_{IOBM} . The velocity potential anomalies with larger negative (positive) loadings in the upper (lower)
341 troposphere are concentrated surrounding the northeast corner of TIO. Under these circumstances, local upper (lower)
342 tropospheric divergence (convergence) and negative (positive) RWS anomalies can be observed (**Fig. 8**), suggesting
343 enhanced ascending motions and convection activities in situ and thereby exciting the localized increased
344 precipitation/atmospheric heating. The above results indicate that IOBM cooling may transmit its interdecadal influence
345 via the intermediate atmospheric bridge of enhanced convective activities around the northeast corner of TIO, exerting a
346 remote modulation on an interdecadal enhancement of the EAMBZ rainfall.

347
348 Next, we further discuss the physical pathway linking IOBM cooling with the far-reaching downstream circulation
349 anomalies responsible for the interdecadal enhancement of EAMBZ precipitation, as shown in **Fig. 9**. Because the
350 cyclonic anomaly at 400 hPa shifts more eastward compared to the I_{EAMBZP} -regressed counterpart (**Fig. 9a** vs. **3a**), only
351 fractional westerly anomalies occupy the eastern part of the westerly-dominated region. The TCC between I_{IOBM} and I_{WI}
352 is nearly equal to zero ($r = -0.06$), thus linking the insignificant cold temperature advection displayed in **Fig. 4c**.
353 Nevertheless, in the lower troposphere, a “north-low–south-high” meridional seesaw pattern over the Northeast China–
354 SWP sector is found to be linked with IOBM cooling (**Fig. 9b**). Note that this negative I_{IOBM} -regressed seesaw pattern
355 exhibits a quasi-barotropic structure, with an anticlockwise $\langle WVT \rangle$ gyre in the north and a SWPCGA in the south (**Fig.**
356 **9c**), which is highly similar to that shown in **Fig. 3**. Significant anomalies of 850-hPa meridional winds and southerly
357 $\langle WVT \rangle$ prevail over the key monsoonal southerly domain, lying on the western flank of SWPCGA (**Figs. 9b** and **c**). The
358 TCC between I_{IOBM} and I_{MI} is -0.33 , significant at 0.05 on interdecadal timescales, thereby linking the significant warm
359 temperature advection anomalies indicated in **Fig. 4d**.

360
361 One may ask how IOBM cooling induces the above-mentioned meridional seesaw pattern. Previously, we have revealed
362 that negative SSTAs over TIO may exert remote interdecadal impacts through an atmospheric bridge, i.e., vigorous
363 convective activities around the northeast corner of TIO (**Figs. 7** and **8**). In effect, there exists a low-level cyclonic
364 anomaly in situ (**Fig. 9b**). Such cyclonic anomaly can be interpreted as a typical Gill–Matsuno-type response (Matsuno,
365 1966; Gill, 1980) to the regional anti-symmetric atmospheric heating caused by IOBM cooling with the coldest center
366 located south of the equator, which is more clear within the lower levels (**Fig. 9b**). As a result, consistent easterly
367 anomalies appear from SWP to its northern flank around 15°N , denoting the active role of depressed air pressure. The
368 consistent easterly anomalies over SWP could lead to local anticyclonic wind shear anomalies (Wang et al., 2019). In
369 such a scenario, a quasi-barotropic SWPCGA can be induced (**Fig. 9c**). Further, local downward motions tied to SWPCGA
370 could induce significant upward motions to its north via a meridional overturning circulation (J. Wang et al., 2021), thus
371 exciting a quasi-barotropic cyclonic anomaly and an anticlockwise $\langle WVT \rangle$ gyre pattern centered over Northeast China
372 (**Figs. 9a–c**). Therefore, positive summertime rainfall anomalies over EAMBZ at interdecadal timescales can be induced
373 (**Fig. 9d**). Notably, circulation and precipitation anomalies during the warm phase years of the IOBM (Fig. S5) highly
374 mirror those tied to the IOBM cooling with opposite signs.

375 **3.4 Results from CESM1 simulations**

376
377
378 In this subsection, we use the pacemaker experimental data based on the ensemble mean of CESM1 IOPES and
379 CESM1 LENS to validate our proposed mechanisms regarding the modulation of IOBM cooling on the interdecadal
380 enhancement of summer EAMBZ precipitation. Considering the predominant role of southerly anomalies over the key

381 monsoonal southerly domain, we therefore emphasize the low-level (850 hPa) atmospheric anomalies at interdecadal
382 timescales tied to the IOBM-like SST cooling, as depicted in Fig. 10. We can observe a clearly anomalous cyclonic
383 circulation around the northeast corner of TIO, accompanied by local positive precipitation anomalies and easterly
384 anomalies that stretch from SWP to its northern flank, which are generally resembled those in the observation (Fig. 9). In
385 this circumstance, a similar “north-low–south-high” meridional seesaw pattern over the Northeast China–SWP sector can
386 be simulated to spark and sustain the enhanced EAMBZ precipitation in boreal summer (Fig. 10). In summary, by and
387 large, the ensemble mean composite results can well reproduce the observed anomalous circulation and precipitation
388 driven by IOBM-related SSTAs, confirming the crucial role of IOBM cooling in driving enhanced summer precipitation
389 over EAMBZ at interdecadal timescales.

390

391 **3.5 Estimation of the interdecadal variations of summer EAMBZ precipitation**

392

393 In the last three subsections, we suggest that the IOBM cooling can serve as a significant oceanic modulator for increased
394 summer EAMBZ precipitation at interdecadal timescales based on observation evidences and pacemaker experiments,
395 and present the corresponding physical mechanisms. To estimate their steady antiphase relationship, in the following, the
396 negative I_{IOBM} is selected to construct a physical-based empirical (**P-E**) model by using the simple linear regression (**SLR**)
397 analysis and the cross-validation method (You and Jia, 2018; Chang et al., 2021; Jeong et al., 2021), representing the
398 impact of IOBM cooling. The **physical-based P-E** model is given as follows:

399

$$400 I_{EAMBZP} = \beta_0 + \beta_1 I_{IOBM} + \varepsilon, \quad (5)$$

401

402 where β_0 and β_1 are regression coefficients, and ε denotes the residuals. The time series of I_{EAMBZP} and I_{IOBM} are detrended
403 and 11-year low-pass filtered beforehand.

404

405 Following the method of Jeong et al. (2021), a “leaving one out” cross-validation strategy is employed to determine the
406 robustness of the hindcast estimates. The normalized time series of summer I_{EAMBZP} and associated leave-one-out cross-
407 validated hindcast estimates are shown in Fig. 11. The TCC between the physical-based P-E predicted hindcast estimates
408 (blue line) and the observed I_{EAMBZP} (red line) for 1901–2014 can reach 0.56 ($P < 0.05$), suggesting that the physical-
409 based P-E model can well capture the interdecadal I_{EAMBZP} variations and reflect their steady relationship.

410

411 Although our proposed physical-based empirical model could confirm the concurrently intimately interdecadal
412 relationship between IOBM and EAMBZ precipitation, we should acknowledge the shortcomings of the model.
413 First, the amplitudes of the hindcast estimates are fairly lower, which cannot well capture the extreme precipitation
414 years (e.g., years around 1960; Fig. 11). Second, the simultaneous signal of IOBM cannot be served as a predictor
415 for summertime EAMBZ precipitation variations. As such, this model inherently lacks the ability to predict the
416 interdecadal EAMBZ precipitation anomalies in advance.

417

418 **4 Conclusions and discussion**

419

420 In this study, by analysis of the long-term observational and reanalysis datasets during 1901–2014, the temporal
421 characteristics of interdecadal variations in the summer EAMBZ precipitation and associated circulation background are
422 revealed. The potential modulation of IOBM on the variations is further discussed. As a summary of our major findings,
423 Fig. 12 schematically synthesizes how IOBM-associated SST mode remotely drives the interdecadal precipitation

424 fluctuations via a tropical route.

425

426 The summer EAMBZ precipitation exhibited a salient interdecadal fluctuations, e.g., with dry summers during the periods
427 preceding 1927, 1939–1945, 1968–1982, and 1998–2010, as well as wet summers during the periods of 1928–1938,
428 1946–1967, and 2011 onwards. It is indicated that the cold airflows brought by the mid-latitude accelerated upstream
429 westerlies over the westerly-dominated domain collide and converge with the warm and humid airflows brought by the
430 enhanced southerlies over the key EASM-controlled domain, suggesting the local extratropical–tropical interplay. Further
431 diagnostic results suggest that the monsoonal southerly anomalies could be viewed as the predominant driving factor for
432 the interdecadal enhancement of EAMBZ precipitation, whereas the upstream westerlies play a secondary dynamical
433 amplification role. Such circulation anomalies are closely linked to a “north-low–south-high” meridional seesaw pattern
434 over the Northeast China–SWP sector, which provides favorable environments for the transportation of water vapor from
435 the SWP and the convergence over EAMBZ to spark enhanced summer EAMBZ precipitation at interdecadal timescales.

436

437 We further identify that the IOBM-related SST anomaly pattern is a salient oceanic modulator for the interdecadal
438 variations of the summer EAMBZ precipitation via the Gill–Matsuno mechanism. When the cold phase of the IOBM
439 occurs, an anomalous cyclonic circulation is excited around the northeast corner of TIO in terms of the regional anti-
440 symmetric atmospheric heating. As a response, consistent easterly anomalies appear from SWP to its northern flank,
441 leading to local anticyclonic wind shear anomalies and thus inducing a SWPCGA pattern and a resultant anticlockwise
442 gyre pattern centered over Northeast China. On interdecadal timescales, such meridional seesaw pattern tied to the IOBM
443 cooling is responsible for enhanced summer precipitation over EAMBZ through linking the predominant driving factor
444 of strengthened monsoonal southerly anomalies west of the SWPCGA pattern. As such, the water vapor transportation
445 from the SWP and the convergence over EAMBZ can be triggered to induce and sustain the enhancement local
446 precipitation. Correspondingly, a physical-based ~~P-E~~ model based the negative I_{IOBM} is constructed, which can well capture
447 the interdecadal fluctuations in the EAMBZ precipitation and reflect their steady relationship. Furthermore, the results
448 based on the large ensemble experiment and the Indian Ocean pacemaker experiment also confirm the crucial physical
449 pathway linking the SST variations over TIO with the summer precipitation over EAMBZ via the influence of SST
450 variations on the aforementioned meridional seesaw pattern at interdecadal timescales.

451

452 The following two points deserve further discussion. First, although results from CESM1 LENS and CESM1 IOPES
453 can reasonably confirm our proposed physical pathway of how IOBM cooling exerts a distant modulation on the
454 interdecadal enhancement of summer precipitation over EAMBZ, we can still notice the weakness of the model
455 simulations. That is, positive precipitation anomalies around the northeast corner of TIO and the easterly anomalies
456 exhibit weaker magnitudes compared to the observations (Fig. 10 vs. 7b and 9b). Besides, systematic biases exist
457 regarding the simulated positions of the upper (lower) tropospheric divergence (convergence) and negative (positive)
458 RWS anomalies (Fig. S6), manifesting themselves in the eastward displacement tendency in contrast to those around the
459 northeast corner of the TIO (Fig. 8).

460

461 Second, this study merely identifies the physical linkage between the interdecadal summer EAMBZ precipitation
462 and the contemporaneous SST mode over the TIO basin from the tropical route. Nonetheless, the contemporaneous
463 IOBM is not a predictor. According to many previous studies (e.g., Wang et al., 2015; Li et al., 2023), the physical-
464 based empirical model based on multiple predictors may better improve the forecast skill. Thus, it is urgent to find
465 out more salient precursor signals of the lower boundary anomalies [e.g., sea ice (Han et al., 2021)] and figure out
466 associated mechanisms for interdecadal EAMBZ precipitation changes to construct an effective prediction model.

467

468 **Code and data availability.** The CRU time series precipitation data version 3.26 (CRU TS3.26) from CRU at the
469 University of East Anglia are available online (<https://catalogue.ceda.ac.uk/uuid/3f894480cc48e1cbc29a5ee12d8542d>;
470 [CRU, 2022](#)). The ERSSTv5 data from the US NOAA are available from the following website:
471 <https://www1.ncdc.noaa.gov/pub/data/cmb/ersst/v5/netcdf/> ([NOAA 2020](#)). The 20CRv2c datasets from NOAA-CIRES
472 are available from the following website: https://psl.noaa.gov/data/gridded/data.20thC_ReanV2c.html ([NOAA-CIRES,](#)
473 [2022](#)). The model simulation datasets regarding CESM1_LENS are available online
474 (<https://www.cesm.ucar.edu/community-projects/lens/data-sets>; [NCAR 2023](#)). The model simulation datasets regarding
475 CESM1_IOPES are available online (<https://www.earthsystemgrid.org/dataset/ucar.cgd.cesm4.IOD-PACEMAKER.html>;
476 [NCAR 2023](#)).

477 Codes are available from the corresponding author on reasonable request.

478

479 **Author contributions.** YL designed the research; JW wrote the first draft of the paper; FC and CS downloaded and
480 analyzed the data, and plotted the figures used in this study. All authors, including YD and XX, contributed to the
481 discussion of the results and reviewed the manuscript.

482

483 **Competing interests.** The contact author has declared that none of the authors has any competing interests.

484

485 **Acknowledgements.** Yanju Liu acknowledges the support by the Key Innovation Team of China Meteorological
486 Administration “Climate Change Detection and Response” (CMA2022ZD03).

487

488 **Financial support.** This study was supported by the Second Tibetan Plateau Scientific Expedition and Research (STEP)
489 program (2019QZKK010204-02 and 2019QZKK0102), Guangdong Major Project of Basic and Applied Basic Research
490 (2020B0301030004), and Innovation and Development Special Project of China Meteorological Administration
491 (CXFZ2022J039).

492

493

494 **References**

495

496 Chang, L., Wu, Z. and Xu, J., 2021. Contribution of Northeastern Asian stratospheric warming to subseasonal prediction
497 of the early winter haze pollution in Sichuan Basin, China. *Science of the Total Environment*, 751: 141823.

498 Chen, F.-H., Chen, J.-H., Holmes, J., Boomer, I., Austin, P., Gates, J.B., Wang, N.-L., Brooks, S.J. and Zhang, J.-W., 2010.
499 Moisture changes over the last millennium in arid central Asia: a review, synthesis and comparison with monsoon
500 region. *Quaternary Science Reviews*, 29(7): 1055-1068.

501 Chen, J., Huang, W., Feng, S., Zhang, Q., Kuang, X., Chen, J. and Chen, F., 2021. The modulation of westerlies-monsoon
502 interaction on climate over the monsoon boundary zone in East Asia. *International Journal of Climatology*,
503 41(S1): E3049-E3064.

504 Chen, J., Huang, W., Jin, L., Chen, J., Chen, S. and Chen, F., 2018. A climatological northern boundary index for the East
505 Asian summer monsoon and its interannual variability. *Science China Earth Sciences*, 61(1): 13-22.

506 Compo, G.P., Whitaker, J.S., Sardeshmukh, P.D., Matsui, N., Allan, R.J., Yin, X., Gleason, B.E., Vose, R.S., Rutledge, G.,
507 Bessemoulin, P., Brönnimann, S., Brunet, M., Crouthamel, R.I., Grant, A.N., Groisman, P.Y., Jones, P.D., Kruk,
508 M.C., Kruger, A.C., Marshall, G.J., Maugeri, M., Mok, H.Y., Nordli, Ø., Ross, T.F., Trigo, R.M., Wang, X.L.,
509 Woodruff, S.D. and Worley, S.J., 2011. The Twentieth Century Reanalysis Project. *Quarterly Journal of the Royal*
510 *Meteorological Society*, 137(654): 1-28.

511 CRU: CRU TS3.26, monthly, CRU [data set] <https://catalogue.ceda.ac.uk/uuid/3f894480cc48e1cbc29a5ee12d8542d>,
512 last access: 5 July 2022.

513 Ding, Y. and Chan, J.C.L., 2005. The East Asian summer monsoon: an overview. *Meteorology and Atmospheric Physics*,
514 89(1): 117-142.

515 Dou, J. and Wu, Z., 2018. Southern Hemisphere origins for interannual variations of snow cover over the western Tibetan
516 Plateau in boreal summer. *Journal of Climate*, 31(19): 7701-7718.

517 Duchon, C.E., 1979. Lanczos filtering in one and two dimensions. *Journal of Applied Meteorology and Climatology*,
518 18(8): 1016-1022.

519 Gill, A.E., 1980. Some simple solutions for heat-induced tropical circulation. *Quarterly Journal of the Royal*
520 *Meteorological Society*, 106(449): 447-462.

521 [Han, T., Zhang, M., Zhu, J., Zhou, B. and Li, S., 2021. Impact of early spring sea ice in Barents Sea on midsummer](#)
522 [rainfall distribution at Northeast China. *Climate Dynamics*, 57\(3\): 1023-1037.](#)

523 Han, W., Vialard, J., McPhaden, M.J., Lee, T., Masumoto, Y., Feng, M. and de Ruijter, W.P.M., 2014. Indian Ocean
524 decadal variability: A review. *Bulletin of the American Meteorological Society*, 95(11): 1679-1703.

525 Harris, I., Jones, P.D., Osborn, T.J. and Lister, D.H., 2014. Updated high-resolution grids of monthly climatic
526 observations—the CRU TS3.10 Dataset. *International Journal of Climatology*, 34(3): 623-642.

527 Henley, B.J., Gergis, J., Karoly, D.J., Power, S., Kennedy, J. and Folland, C.K., 2015. A Tripole Index for the Interdecadal
528 Pacific Oscillation. *Climate Dynamics*, 45(11): 3077-3090.

529 Huang, B., Thorne, P.W., Banzon, V.F., Boyer, T., Chepurin, G., Lawrimore, J.H., Menne, M.J., Smith, T.M., Vose, R.S.
530 and Zhang, H.-M., 2017. Extended Reconstructed Sea Surface Temperature, version 5 (ERSSTv5): Upgrades,
531 validations, and intercomparisons. *Journal of Climate*, 30(20): 8179-8205.

532 Huang, J., Li, Y., Fu, C., Chen, F., Fu, Q., Dai, A., Shinoda, M., Ma, Z., Guo, W., Li, Z., Zhang, L., Liu, Y., Yu, H., He,
533 Y., Xie, Y., Guan, X., Ji, M., Lin, L., Wang, S., Yan, H. and Wang, G., 2017. Dryland climate change: Recent
534 progress and challenges. *Reviews of Geophysics*, 55(3): 719-778.

535 Huang, J., Ma, J., Guan, X., Li, Y. and He, Y., 2019. Progress in semi-arid climate change studies in China. *Advances in*
536 *Atmospheric Sciences*, 36(9): 922-937.

537 Huang, J., Zhang, G., Zhang, Y., Guan, X., Wei, Y. and Guo, R., 2020. Global desertification vulnerability to climate
538 change and human activities. *Land Degradation & Development*, 31(11): 1380-1391.

539 Huang, W., Chen, J., Zhang, X., Feng, S. and Chen, F., 2015. Definition of the core zone of the “westerlies-dominated
540 climatic regime”, and its controlling factors during the instrumental period. *Science China Earth Sciences*, 58(5):
541 676-684.

542 Huang, Y., Wu, B., Li, T., Zhou, T. and Liu, B., 2019. Interdecadal Indian Ocean basin mode driven by interdecadal
543 Pacific oscillation: A season-dependent growth mechanism. *Journal of Climate*, 32(7): 2057-2073.

544 Hurrell, J.W., Holland, M.M., Gent, P.R., Ghan, S., Kay, J.E., Kushner, P.J., Lamarque, J.F., Large, W.G., Lawrence, D.,
545 Lindsay, K., Lipscomb, W.H., Long, M.C., Mahowald, N., Marsh, D.R., Neale, R.B., Rasch, P., Vavrus, S.,
546 Vertenstein, M., Bader, D., Collins, W.D., Hack, J.J., Kiehl, J. and Marshall, S., 2013. The Community Earth
547 System Model: A framework for collaborative research. *Bulletin of the American Meteorological Society*, 94(9):
548 1339-1360.

549 Jeong, J.I., Park, R.J., Yeh, S.-W. and Roh, J.-W., 2021. Statistical predictability of wintertime PM_{2.5} concentrations over
550 East Asia using simple linear regression. *Science of the Total Environment*, 776: 146059.

551 Jiang, J., Zhou, T., Chen, X. and Wu, B., 2021. Central Asian precipitation shaped by the tropical Pacific decadal
552 variability and the Atlantic multidecadal variability. *Journal of Climate*, 34(18): 7541-7553.

553 Kay, J.E., Deser, C., Phillips, A., Mai, A., Hannay, C., Strand, G., Arblaster, J.M., Bates, S.C., Danabasoglu, G., Edwards,
554 J., Holland, M., Kushner, P., Lamarque, J.F., Lawrence, D., Lindsay, K., Middleton, A., Munoz, E., Neale, R.,
555 Oleson, K., Polvani, L. and Vertenstein, M., 2015. The community earth system model (CESM) large ensemble
556 project: a community resource for studying climate change in the presence of internal climate variability. *Bulletin*
557 *of the American Meteorological Society*, 96(8): 1333-1349.

558 Klein, S.A., Soden, B.J. and Lau, N.-C., 1999. Remote sea surface temperature variations during ENSO: evidence for a
559 tropical atmospheric bridge. *Journal of Climate*, 12(4): 917-932.

560 Li, J., Sun, C. and Jin, F.-F., 2013. NAO implicated as a predictor of Northern Hemisphere mean temperature multidecadal
561 variability. *Geophysical Research Letters*, 40(20): 5497-5502.

562 Li, J. and Zeng, Q., 2002. A unified monsoon index. *Geophysical Research Letters*, 29(8): 115-1-115-4.

563 [Li, J., Zheng, C., Yang, Y., Lu, R. and Zhu, Z., 2023. Predictability of spatial distribution of pre-summer extreme](#)
564 [precipitation days over southern China revealed by the physical-based empirical model. *Climate Dynamics*,](#)
565 [61\(5\): 2299-2316.](#)

566 Li, M. and Ma, Z., 2018. Decadal changes in summer precipitation over arid northwest China and associated atmospheric
567 circulations. *International Journal of Climatology*, 38(12): 4496-4508.

568 Lu, W. and Jia, G., 2013. Fluctuation of farming-pastoral ecotone in association with changing East Asia monsoon climate.
569 *Climatic Change*, 119(3): 747-760.

570 Mastyo, M., 2013. Bilinear interpolation theorems and applications. *Journal of Functional Analysis*, 265(2): 185-207.

571 Matsuno, T., 1966. Quasi-geostrophic motions in the equatorial area. *Journal of the Meteorological Society of Japan*,

572 44(1): 25-43.

573 Moss, R.H., Edmonds, J.A., Hibbard, K.A., Manning, M.R., Rose, S.K., van Vuuren, D.P., Carter, T.R., Emori, S.,

574 Kainuma, M., Kram, T., Meehl, G.A., Mitchell, J.F.B., Nakicenovic, N., Riahi, K., Smith, S.J., Stouffer, R.J.,

575 Thomson, A.M., Weyant, J.P. and Wilbanks, T.J., 2010. The next generation of scenarios for climate change

576 research and assessment. *Nature*, 463(7282): 747-756.

577 NCAR: CESM1_LENS, monthly, NCAR [data set] <https://www.cesm.ucar.edu/community-projects/lens/data-sets>, last

578 access: 28 April 2023.

579 NCAR: CESM1_IOPES, monthly, NCAR [data set] [https://www.earthsystemgrid.org/dataset/ucar.cgd.cesm4.IOD-](https://www.earthsystemgrid.org/dataset/ucar.cgd.cesm4.IOD-PACEMAKER.html)

580 [PACEMAKER.html](https://www.earthsystemgrid.org/dataset/ucar.cgd.cesm4.IOD-PACEMAKER.html), last access: 4 May 2023.

581 NOAA: ERSSTv5, monthly, NOAA [data set] <https://www1.ncdc.noaa.gov/pub/data/cmb/ersst/v5/netcdf/>, last access: 15

582 October 2020.

583 NOAA-CIRES: 20CRv2c, monthly, NOAA-CIRES [data set]

584 https://psl.noaa.gov/data/gridded/data.20thC_ReanV2c.html, last access: 26 June 2022.

585 North, G.R., Bell, T.L., Cahalan, R.F. and Moeng, F.J., 1982. Sampling errors in the estimation of empirical orthogonal

586 functions. *Monthly Weather Review*, 110(7): 699-706.

587 Ou, T.H. and Qian, W.H., 2006. Vegetation variations along the monsoon boundary zone in East Asia. *Chinese Journal of*

588 *Geophysics (in Chinese)*, 49(3): 698–705.

589 Piao, J., Chen, W. and Chen, S., 2021. Water vapour transport changes associated with the interdecadal decrease in the

590 summer rainfall over Northeast Asia around the late-1990s. *International Journal of Climatology*, 41(S1): E1469-

591 E1482.

592 Qian, W., Ding, T., Hu, H., Lin, X. and Qin, A., 2009. An overview of dry-wet climate variability among monsoon-

593 westerly regions and the monsoon northernmost marginal active zone in China. *Advances in Atmospheric*

594 *Sciences*, 26(4): 630-641.

595 Sardeshmukh, P.D. and Hoskins, B.J., 1988. The generation of global rotational flow by steady idealized tropical

596 divergence. *Journal of Atmospheric Sciences*, 45(7): 1228-1251.

597 Schiemann, R., Lüthi, D. and Schär, C., 2009. Seasonality and interannual variability of the westerly jet in the Tibetan

598 Plateau region. *Journal of Climate*, 22(11): 2940-2957.

599 Si, D. and Ding, Y., 2016. Oceanic forcings of the interdecadal variability in East Asian summer rainfall. *Journal of*

600 *Climate*, 29(21): 7633-7649.

601 Si, D., Jiang, D., Hu, A. and Lang, X., 2021. Variations in northeast Asian summer precipitation driven by the Atlantic

602 multidecadal oscillation. *International Journal of Climatology*, 41(3): 1682-1695.

603 Song, C., Wang, J., Liu, Y., Zhang, L., Ding, Y., Li, Q., Shen, X., Song, Y. and Yan, Y., 2022. Toward role of westerly-

604 monsoon interplay in linking interannual variations of late spring precipitation over the southeastern Tibetan

605 Plateau. *Atmospheric Science Letters*, 23(3): e1074.

606 Sun, B., Li, H. and Zhou, B., 2019a. Interdecadal variation of Indian Ocean basin mode and the impact on Asian summer

607 climate. *Geophysical Research Letters*, 46(21): 12388-12397.

608 Sun, B., Wang, H., Zhou, B. and Li, H., 2019b. Interdecadal variation in the synoptic features of mei-yu in the Yangtze

609 River valley region and relationship with the Pacific decadal oscillation. *Journal of Climate*, 32(19): 6251-6270.

610 Taylor, K.E., Stouffer, R.J. and Meehl, G.A., 2012. An overview of CMIP5 and the experiment design. *Bulletin of the*

611 *American Meteorological Society*, 93(4): 485-498.

612 Touma, D., Stevenson, S., Lehner, F. and Coats, S., 2021. Human-driven greenhouse gas and aerosol emissions cause

613 distinct regional impacts on extreme fire weather. *Nature Communications*, 12(1): 212.

614 Wang, B., Wu, Z., Li, J., Liu, J., Chang, C.-P., Ding, Y. and Wu, G., 2008. How to measure the strength of the East Asian

615 summer monsoon. *Journal of Climate*, 21(17): 4449-4463.

616 [Wang, B., Xiang, B., Li, J., Webster, P.J., Rajeevan, M.N., Liu, J. and Ha, K.-J., 2015. Rethinking Indian monsoon rainfall](#)

617 [prediction in the context of recent global warming. *Nature Communications*, 6\(1\): 7154.](#)

618 Wang, J., Zhu, Z.W., Qi, L., Zhao, Q.H., He, J.H. and Wang, J.X.L., 2019. Two pathways of how remote SST anomalies

619 drive the interannual variability of autumnal haze days in the Beijing–Tianjin–Hebei region, China. *Atmospheric*

620 *Chemistry and Physics*, 19(3): 1521-1535.

621 Wang, J., Liu, Y., Ding, Y. and Wu, Z., 2021. Towards influence of Arabian Sea SST anomalies on the withdrawal date of

622 Meiyu over the Yangtze-Huaihe River basin. *Atmospheric Research*, 249: 105340.

623 Wang, J., Liu, Y., Song, C., Ding, Y., Li, Q., Wu, P., Xu, Y. and Xu, X., 2022. Synergistic impacts of westerlies and

624 monsoon on interdecadal variations of late spring precipitation over the southeastern extension of the Tibetan

625 Plateau. *International Journal of Climatology*, 42(14): 7342-7361.

626 Wang, J., Liu, Y., Yang, Y., Wu, P., Yang, J., Liang, P., Song, C., Zhang, S. and Ding, Y., 2023. Impact of early winter
627 North Atlantic Oscillation on the dramatic alternation of seesaw haze intensity between late winter months in
628 the North China Plain. *Atmospheric Research*, 281: 106483.

629 Wang, L., Chen, W., Huang, G. and Zeng, G., 2017. Changes of the transitional climate zone in East Asia: past and future.
630 *Climate Dynamics*, 49(4): 1463-1477.

631 Wang, Q., Wang, L., Huang, G., Piao, J. and Chotamonsak, C., 2021. Temporal and spatial variation of the transitional
632 climate zone in summer during 1961–2018. *International Journal of Climatology*, 41(3): 1633-1648.

633 Wang, Q., Wang, L., Huang, G. and Wang, T., 2022. Mechanism of the summer rainfall interannual variability in
634 transitional climate zone in East Asia: roles of teleconnection patterns and associated moisture processes.
635 *Climate Dynamics*, <https://doi.org/10.1007/s00382-022-06618-1>.

636 Wang, Q., Huang, G., Wang, L., Piao, J., Ma, T., Hu, P., Chotamonsak, C. and Limsakul, A., 2023. Mechanism of the
637 summer rainfall variation in Transitional Climate Zone in East Asia from the perspective of moisture supply
638 during 1979–2010 based on the Lagrangian method. *Climate Dynamics*, 60(3): 1225-1238.

639 Wang, S., Huang, J., Huang, G., Luo, F., Ren, Y. and He, Y., 2022. Enhanced impacts of Indian Ocean sea surface
640 temperature on the dry/wet variations over Northwest China. *Journal of Geophysical Research: Atmospheres*,
641 127(11): e2022JD036533.

642 Wu, B., Zhou, T. and Li, T., 2016. Impacts of the Pacific–Japan and circumglobal teleconnection patterns on the
643 interdecadal variability of the East Asian summer monsoon. *Journal of Climate*, 29(9): 3253-3271.

644 Wu, G., Guan, Y., Liu, Y., Yan, J. and Mao, J., 2012. Air–sea interaction and formation of the Asian summer monsoon
645 onset vortex over the Bay of Bengal. *Climate Dynamics*, 38(1): 261-279.

646 Wu, P., Liu, Y., Ding, Y., Li, X. and Wang, J., 2022. Modulation of sea surface temperature over the North Atlantic and
647 Indian-Pacific warm pool on interdecadal change of summer precipitation over northwest China. *International
648 Journal of Climatology*, 42(16): 8526-8538.

649 Xie, S.-P., Hu, K., Hafner, J., Tokinaga, H., Du, Y., Huang, G. and Sampe, T., 2009. Indian Ocean capacitor effect on
650 Indo–western Pacific climate during the summer following El Niño. *Journal of Climate*, 22(3): 730-747.

651 Xing, W. and Wang, B., 2017. Predictability and prediction of summer rainfall in the arid and semi-arid regions of China.
652 *Climate Dynamics*, 49(1): 419-431.

653 Yang, D., Arblaster, J.M., Meehl, G.A., England, M.H., Lim, E.-P., Bates, S. and Rosenbloom, N., 2020. Role of tropical
654 variability in driving decadal shifts in the Southern Hemisphere summertime eddy-driven jet. *Journal of Climate*,
655 33(13): 5445-5463.

656 Yang, J., Liu, Q., Xie, S.-P., Liu, Z. and Wu, L., 2007. Impact of the Indian Ocean SST basin mode on the Asian summer
657 monsoon. *Geophysical Research Letters*, 34(2): L02708.

658 Yeh, T.-C., Dao, S.-Y. and Li, M.-T., 1959. The abrupt change of circulation over the Northern Hemisphere during June
659 and October. *The Atmosphere and the Sea in Motion*, the Rockefeller Institute Press and Oxford University Press,
660 249-267.

661 Ying, K., Jiang, D., Zheng, X., Frederiksen, C.S., Peng, J., Zhao, T. and Zhong, L., 2023. Seasonal predictable source of
662 the East Asian summer monsoon rainfall in addition to the ENSO–AO. *Climate Dynamics*, 60(7): 2459-2480.

663 You, Y. and Jia, X., 2018. Interannual variations and prediction of spring precipitation over China. *Journal of Climate*,
664 31(2): 655-670.

665 Zeng, J. and Zhang, Q., 2019. A humidity index for the summer monsoon transition zone in East Asia. *Climate Dynamics*,
666 53(9): 5511-5527.

667 Zhang, L., Han, W., Karnauskas, K.B., Meehl, G.A., Hu, A., Rosenbloom, N. and Shinoda, T., 2019. Indian Ocean
668 warming trend reduces Pacific warming response to anthropogenic greenhouse gases: An interbasin thermostat
669 mechanism. *Geophysical Research Letters*, 46(19): 10882-10890.

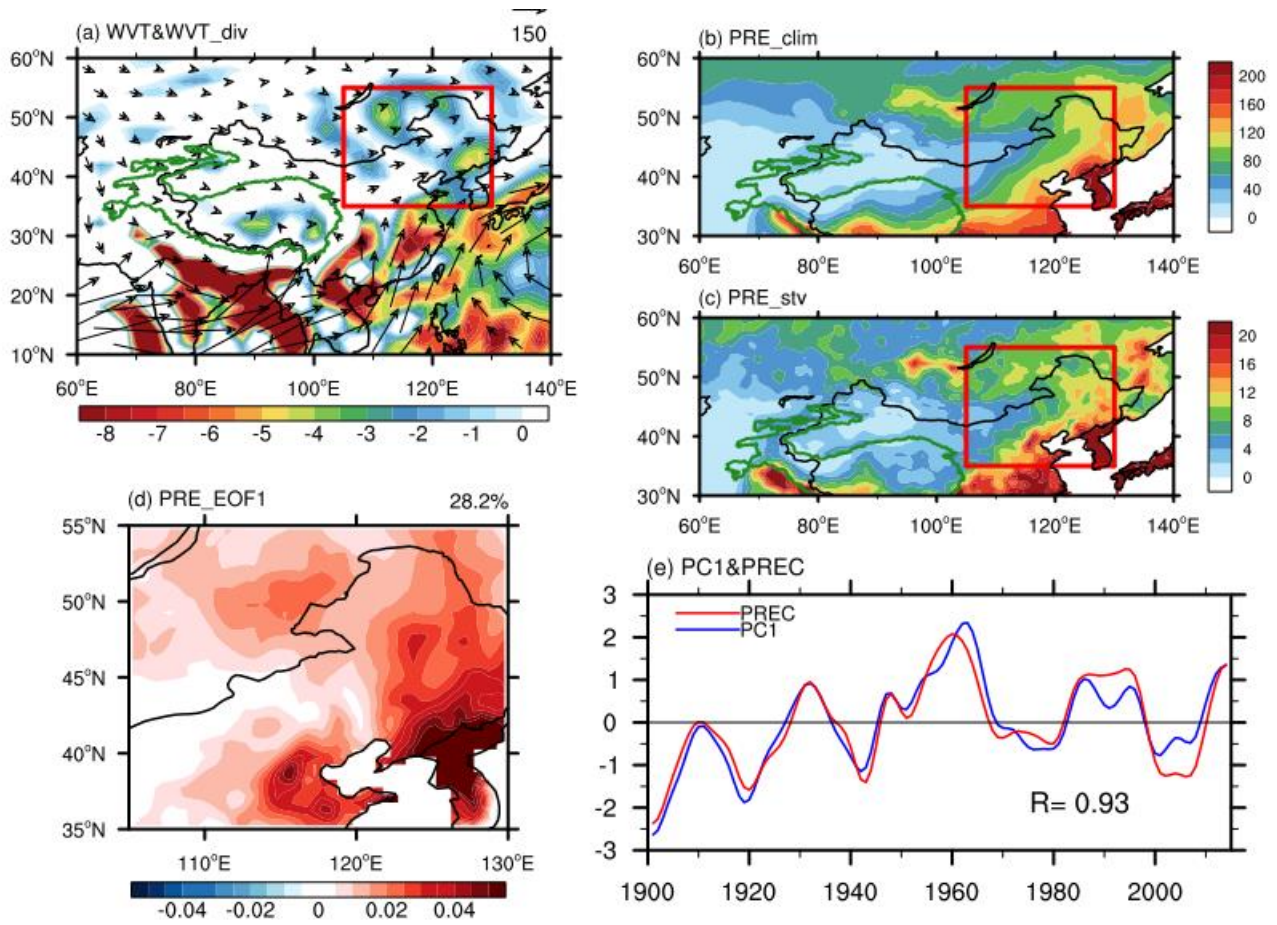
670 Zhang, Z., Sun, X. and Yang, X.-Q., 2018. Understanding the interdecadal variability of East Asian summer monsoon
671 precipitation: Joint influence of three oceanic signals. *Journal of Climate*, 31(14): 5485-5506.

672 Zhao, W., Chen, S., Chen, W., Yao, S., Nath, D. and Yu, B., 2019a. Interannual variations of the rainy season withdrawal
673 of the monsoon transitional zone in China. *Climate Dynamics*, 53(3): 2031-2046.

674 Zhao, W., Chen, W., Chen, S., Yao, S.-L. and Nath, D., 2019b. Inter-annual variations of precipitation over the monsoon
675 transitional zone in China during August–September: Role of sea surface temperature anomalies over the
676 tropical Pacific and North Atlantic. *Atmospheric Science Letters*, 20(1): e872.

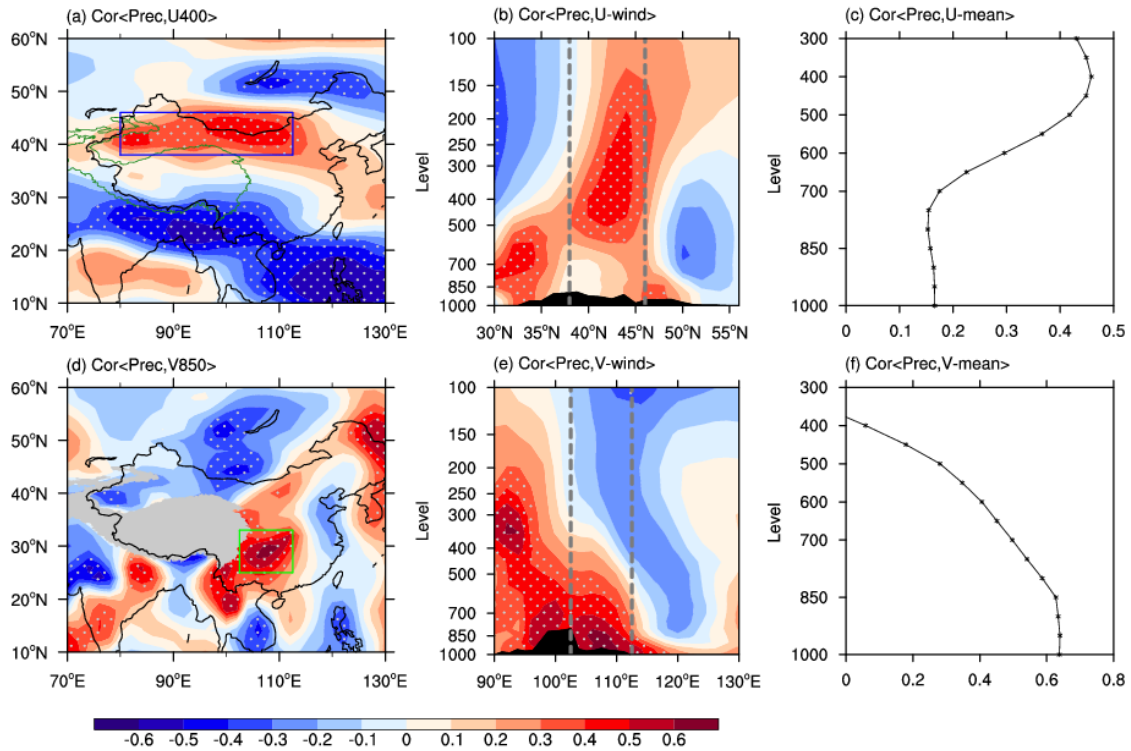
677 Zhao, W., Chen, W., Chen, S., Nath, D. and Wang, L., 2020. Interdecadal change in the impact of North Atlantic SST on
678 August rainfall over the monsoon transitional belt in China around the late 1990s. *Theoretical and Applied
679 Climatology*, 140(1): 503-516.

680 **Figures**
 681



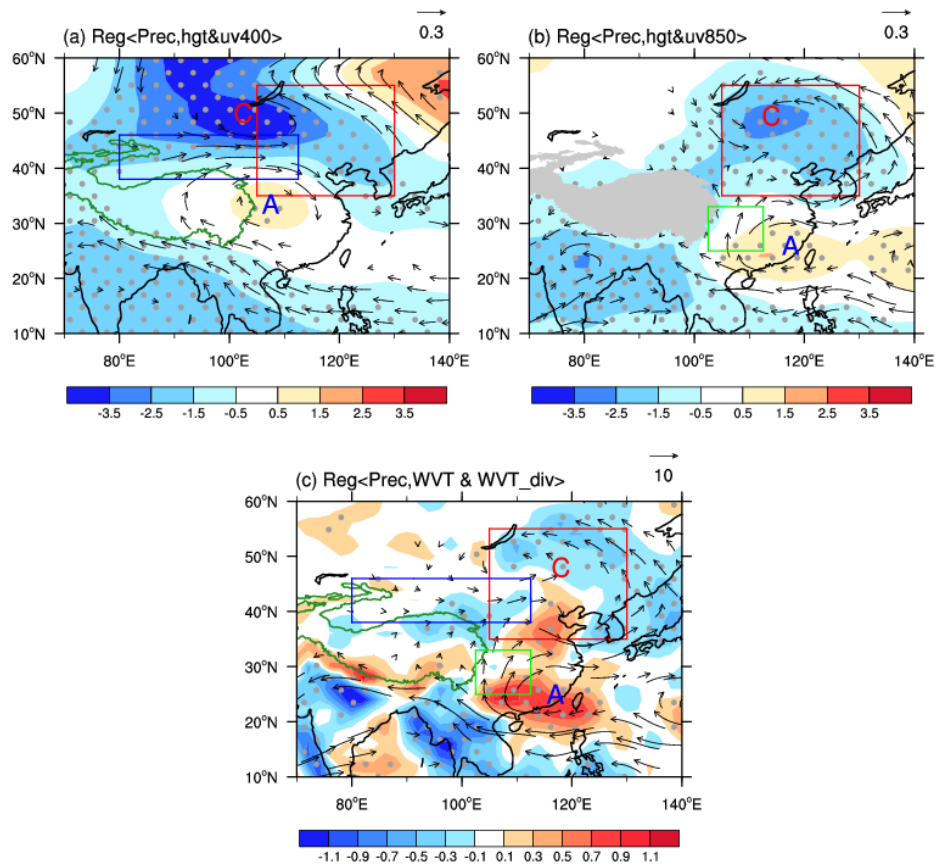
682
 683 **Figure 1.** The climatological JJA-averaged (a) $\langle \text{WVT} \rangle$ (vectors; $\text{kg m}^{-1} \text{s}^{-1}$) and $\langle \text{WVT_div} \rangle$ (shading; $10^{-5} \text{ kg m}^{-2} \text{ s}^{-1}$), (b)
 684 precipitation (mm month^{-1}), and (c) interdecadal standard deviation of precipitation (mm month^{-1}) during the period 1901–2014. The
 685 red box (35° – 55°N , 105° – 130°E) outlines the research domain of EAMBZ (the same hereinafter). (d) Spatial pattern of the first
 686 empirical orthogonal function (EOF1) mode of JJA-mean EAMBZ precipitation. (e) Normalized time series of the JJA-mean EAMBZ
 687 precipitation index (I_{EAMBZP}) (red line) and associated first principal component (PC1) (blue line), with the number denoting the
 688 temporal correlation coefficient (TCC) between the corresponding time series. In panels (c)–(e), variables are detrended and 11-year
 689 low-pass filtered. The green outline in panels (a)–(c) represents the terrain of the Tibetan Plateau (TP) at 2000 m (the same hereinafter).
 690 The precipitation is derived from the CRU TS3.26 precipitation data, while other variables are from the 20CRv2c datasets.

691
 692
 693
 694
 695



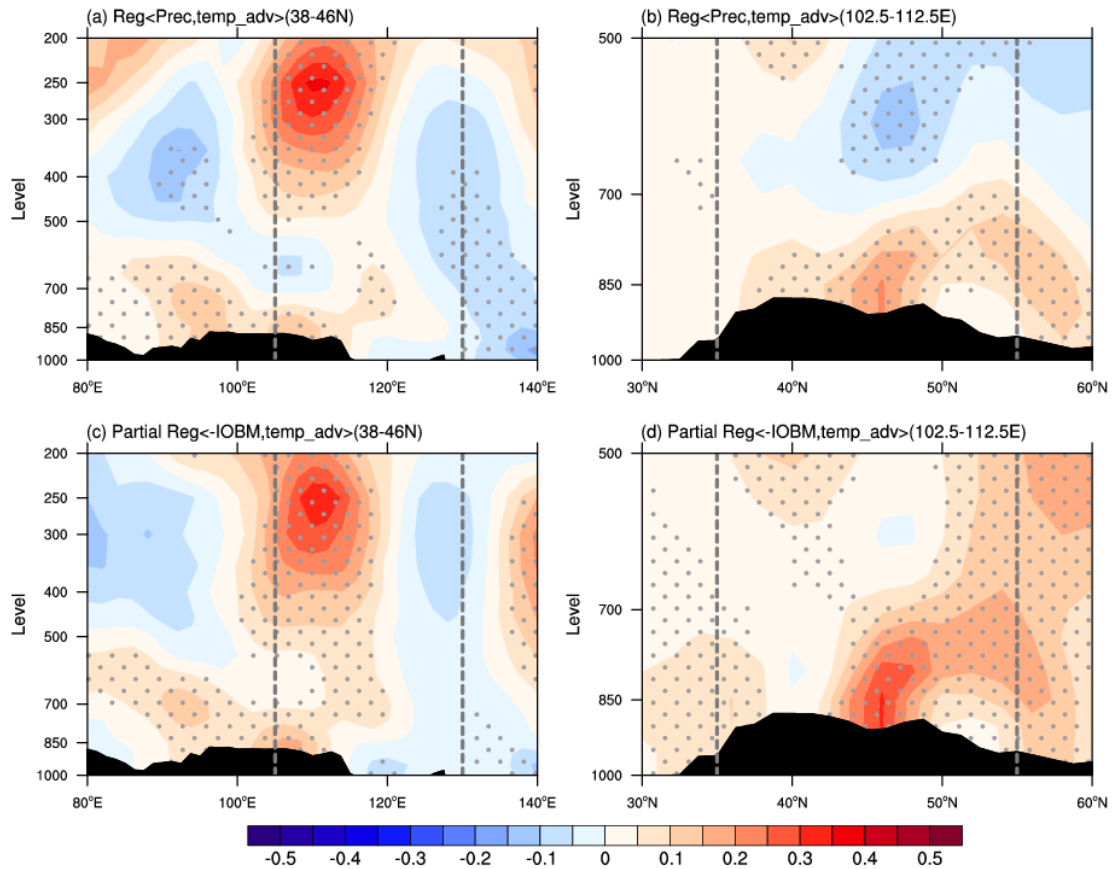
696
697
698
699
700
701
702
703
704
705
706
707
708
709
710
711
712
713
714
715
716
717
718
719

Figure 2. Correlation maps of the JJA-averaged I_{EAMBZP} with the simultaneous (a) 400-hPa zonal wind (U_{400}) and (d) 850-hPa meridional wind (V_{850}), and (b) height–latitude cross-section of zonal winds averaged over 80° – 112.5° E, and (e) height–longitude cross-section of meridional winds averaged over 25° – 33° N, during the period 1901–2014. The blue box (38° – 46° N, 80° – 112.5° E) in (a) and the green box (25° – 33° N, 102.5° – 112.5° E) in (d) represent the upstream westerly domain and the monsoonal southerly domain significantly tied to the interdecadal variations of precipitation over EAMBZ, respectively (the same hereinafter). The grey-dashed vertical lines in (b) and (e) represent the latitudinal and longitudinal range of the westerly and the monsoonal southerly domain, respectively. (c) Profile of correlation coefficients between the JJA-averaged I_{EAMBZP} and the simultaneous area-averaged zonal winds over the upstream westerly domain at multiple levels during the period 1901–2014. (f) As in (c), but for the meridional winds over the monsoonal southerly domain. All variables are detrended and 11-year low-pass filtered. Areas with significant values exceeding the 95% confidence level are stippled. The black shading indicates the topography. The grey shaded areas denote the TP areas above 2000 m (the same hereinafter). The I_{EAMBZP} is calculated based on the CRU TS3.26 precipitation data, while other variables are from the 20CRv2c datasets.



720
 721 **Figure 3.** Regression maps of the JJA-mean anomalies of (a) 400-hPa geopotential height (Z400; shading; m) and wind field (UV400;
 722 vectors; m s^{-1}), (b) 850-hPa geopotential height (Z850; shading; m) and wind field (UV850; vectors; m s^{-1}), and (c) $\langle \text{WVT} \rangle$ (vectors;
 723 $\text{kg m}^{-1} \text{s}^{-1}$) and $\langle \text{WVT}_{\text{div}} \rangle$ (shading; $10^{-5} \text{ kg m}^{-2} \text{s}^{-1}$) onto the concurrent I_{EAMBZP} during the period 1901–2014. All variables are
 724 detrended and 11-year low-pass filtered. Letter A (C) represents the center of anticyclonic (cyclonic) anomaly (the same hereinafter).
 725 Areas with significant values of Z400, Z850, and $\langle \text{WVT}_{\text{div}} \rangle$ that exceed the 95% confidence level are stippled, respectively. Only
 726 vectors that are significant at the 95% confidence level are shown. The I_{EAMBZP} is calculated based on the CRU TS3.26 precipitation
 727 data, while other variables are from the 20CRv2c datasets.

728
 729
 730
 731
 732
 733
 734
 735
 736
 737
 738
 739
 740



741

742

743

744

745

746

747

748

749

750

751

752

753

754

755

756

757

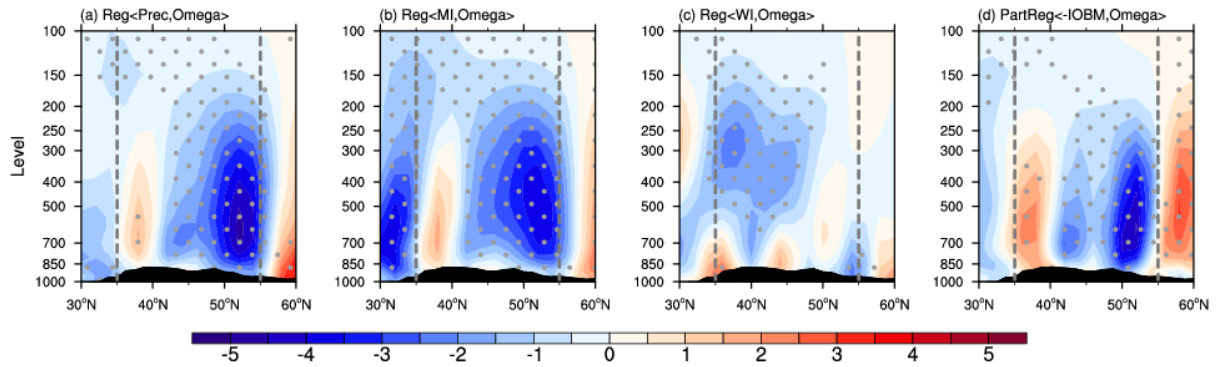
758

759

760

761

Figure 4. (a) Height–longitude cross-section (averaged over 38°–46°N) and (b) height–latitude cross-section (averaged over 102.5°–112.5°E) of the JJA-mean temperature advection anomalies (shading; 10^{-5} K s^{-1}) regressed onto the concurrent I_{EAMBZP} during the period 1901–2014. (c, d) As in (a, b), but for patterns of the partial regression coefficient between temperature advection and negative I_{IOBM} without the IPO signal. The gray vertical lines in (a, c) and (b, d) represent the longitudinal and latitudinal range of the research domain of EAMBZ, respectively. The black shading indicates the topography. All variables are detrended and 11-year low-pass filtered. Areas with significant values exceeding the 95% confidence level are stippled. The I_{EAMBZP} and I_{IOBM}/IPO index are calculated based on the CRU TS3.26 precipitation data and the ERSSTv5 dataset, respectively; whilst other variables are from the 20CRv2c datasets.



762

763 **Figure 5.** Height–latitude cross-section (averaged over 105°–130°E) of the JJA-mean vertical velocity anomalies (10^{-3}Pa s^{-1}) regressed
 764 onto the concurrent (a) I_{EAMBZP} , (b) I_{MI} , and (c) I_{WI} during the period 1901–2014. (d) As in (a), but for the partial regressed anomalies
 765 onto the negative I_{IOBM} with the IPO signal removed. The gray vertical lines represent the latitudinal range of EAMBZ. The black
 766 shading indicates the topography. All variables are detrended and 11-year low-pass filtered. Areas with significant values exceeding
 767 the 95% confidence level are stippled. The I_{EAMBZP} and $I_{\text{IOBM/IPO}}$ index are calculated based on the CRU TS3.26 precipitation data
 768 and the ERSSTv5 dataset, respectively; whilst other variables are from the 20CRv2c datasets.

769

770

771

772

773

774

775

776

777

778

779

780

781

782

783

784

785

786

787

788

789

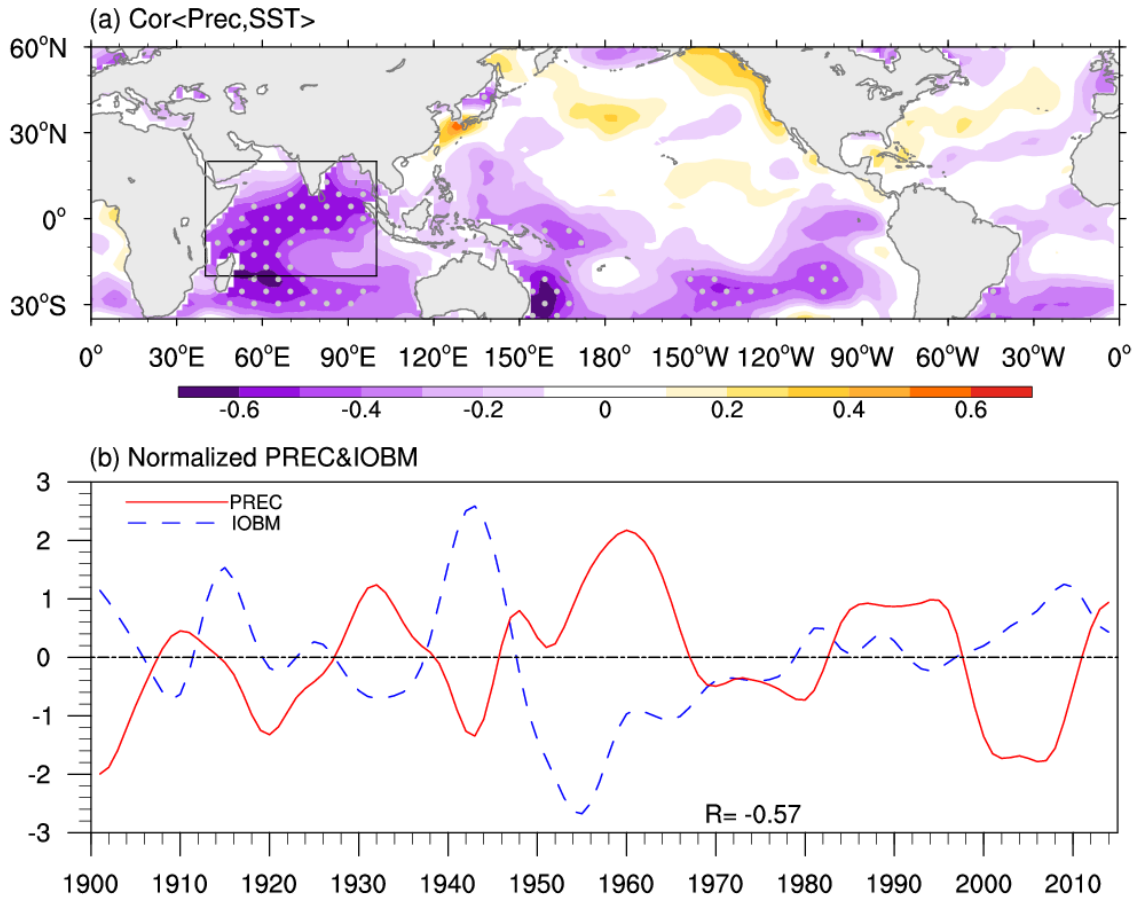
790

791

792

793

794



795

796

797

798

799

800

801

802

803

804

805

806

807

808

809

810

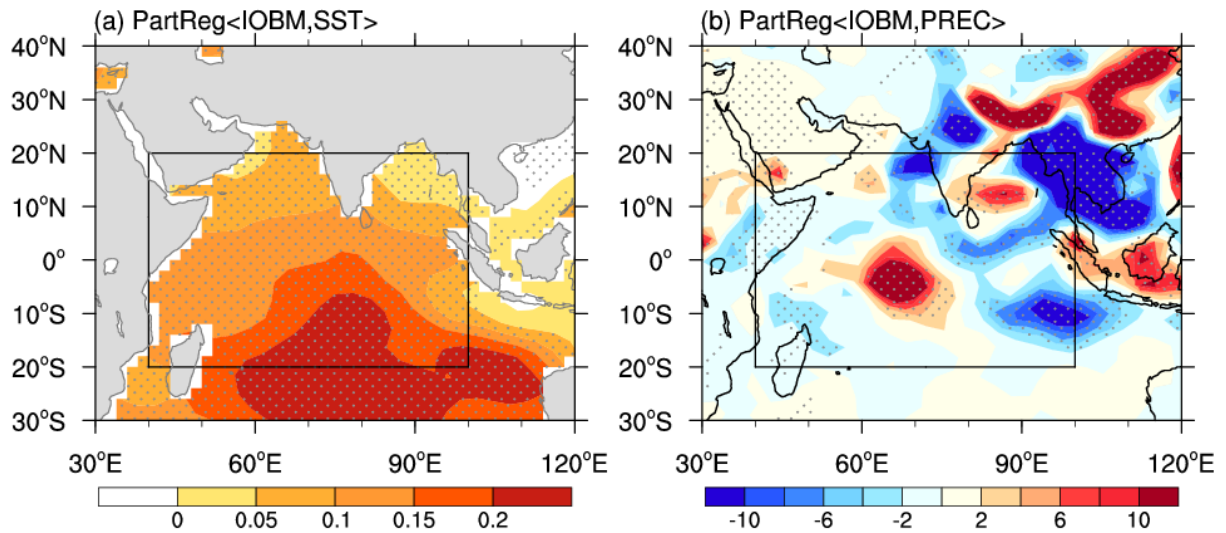
811

812

813

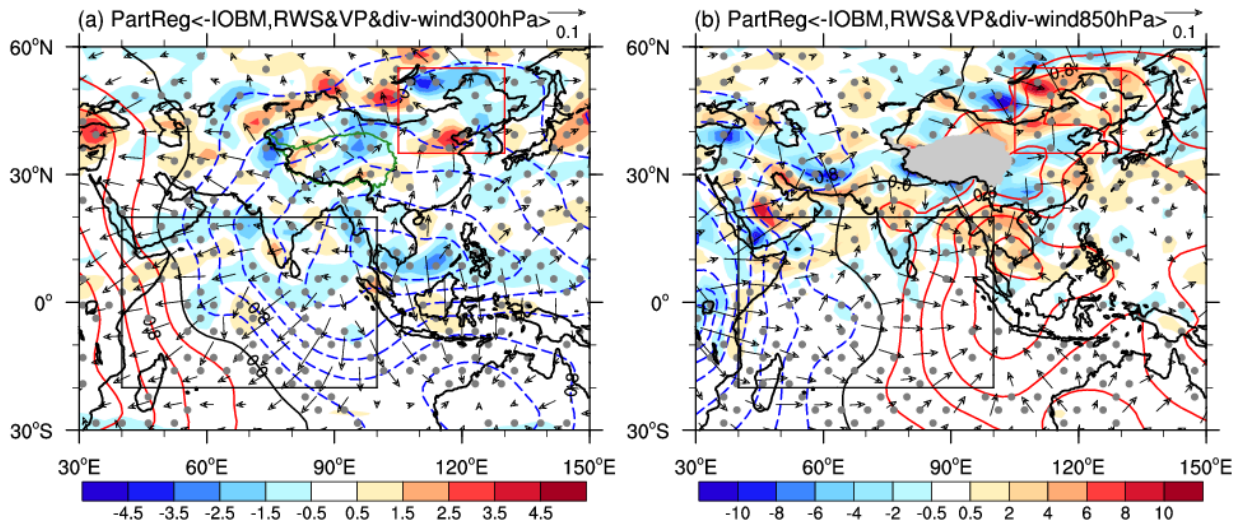
814

Figure 6. (a) Correlation map of the JJA-mean I_{EAMBZP} with the concurrent near-global SST (35°S–60°N) during the period 1901–2014. The black frame (20°S–20°N, 40°–100°E) outlines the domain for delineating the IOBM mode (the same hereinafter). Areas with significant values exceeding the 99% confidence level are hatched/stippled. (b) Normalized time series of the JJA-mean I_{EAMBZP} (red line) and I_{IOBM} (blue line) from 1901 to 2014. The numeral at the bottom represents the TCC between the corresponding time series. All variables are detrended and 11-year low-pass filtered. The SST is from the ERSSTv5 dataset. The I_{EAMBZP} and I_{IOBM} are calculated based on the CRU TS3.26 precipitation data and the ERSSTv5 datasets, respectively.



815
 816 **Figure 7.** Partial regression of the JJA-mean (a) SST (°C) and (b) precipitation (mm month⁻¹) anomalies over TIO and its neighboring
 817 areas onto the concurrent I_{IOBM} with the IPO signal removed for the period 1901–2014. All variables are detrended and 11-year low-
 818 pass filtered. Areas with significant values exceeding the 95% confidence level are stippled. The I_{IOBM} /IPO index is calculated based
 819 on the ERSSTv5 dataset. The SST and the precipitation are derived from the ERSSTv5 dataset and the 20CRv2c dataset, respectively.

820
 821
 822
 823
 824
 825
 826
 827
 828
 829
 830
 831
 832
 833
 834
 835
 836



837

838

839

840

841

842

843

844

845

846

847

848

849

850

851

852

853

854

855

856

857

858

859

860

861

862

863

864

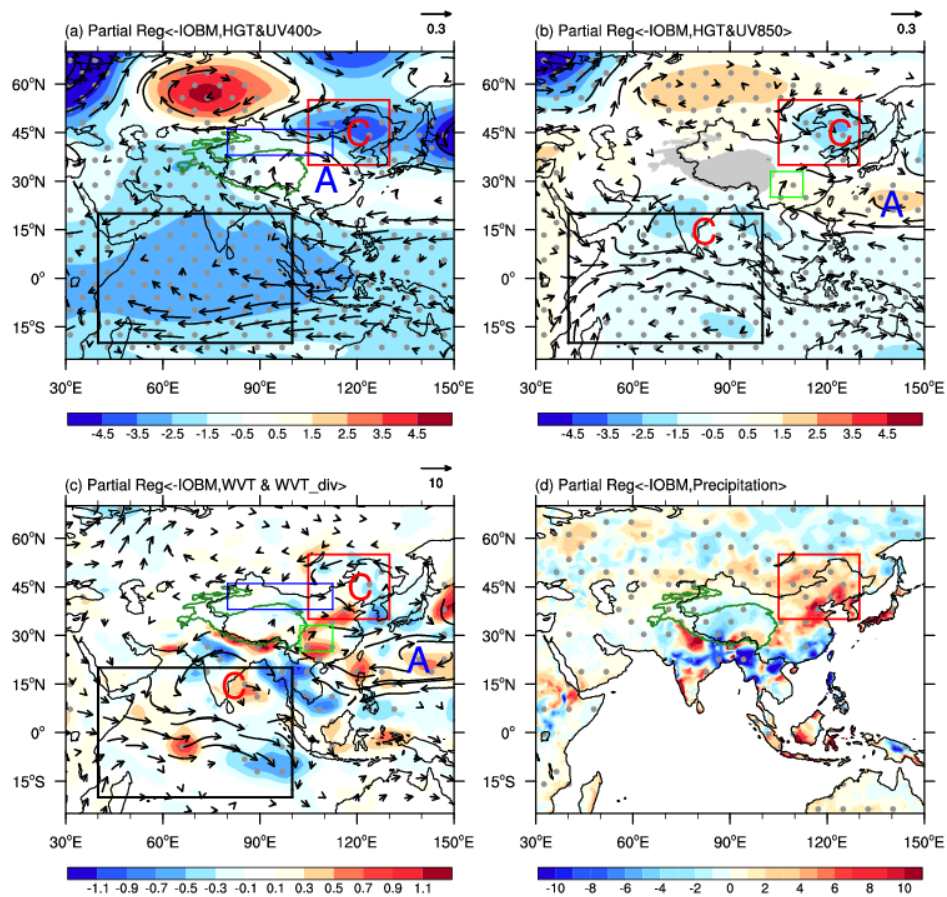
865

866

867

868

Figure 8. Partial regression of the JJA-mean (a) 300- and (b) 850-hPa RWS (shading; 10^{-11} s^{-2}), velocity potential (contours; interval: $0.4; 10^5 \text{ m}^2 \text{ s}^{-1}$), and divergent horizontal wind (vectors; m s^{-1}) anomalies against the concurrent negative I_{IOBM} with the IPO signal removed during the period 1901–2014. All variables are detrended and 11-year low-pass filtered. Areas with significant values of RWS exceeding the 95% confidence level are stippled. The I_{IOBM} /IPO index is calculated based on the ERSSTv5 dataset; whilst other variables are from the 20CRv2c datasets.



869

870

871

872

873

874

875

876

877

878

879

880

881

882

883

884

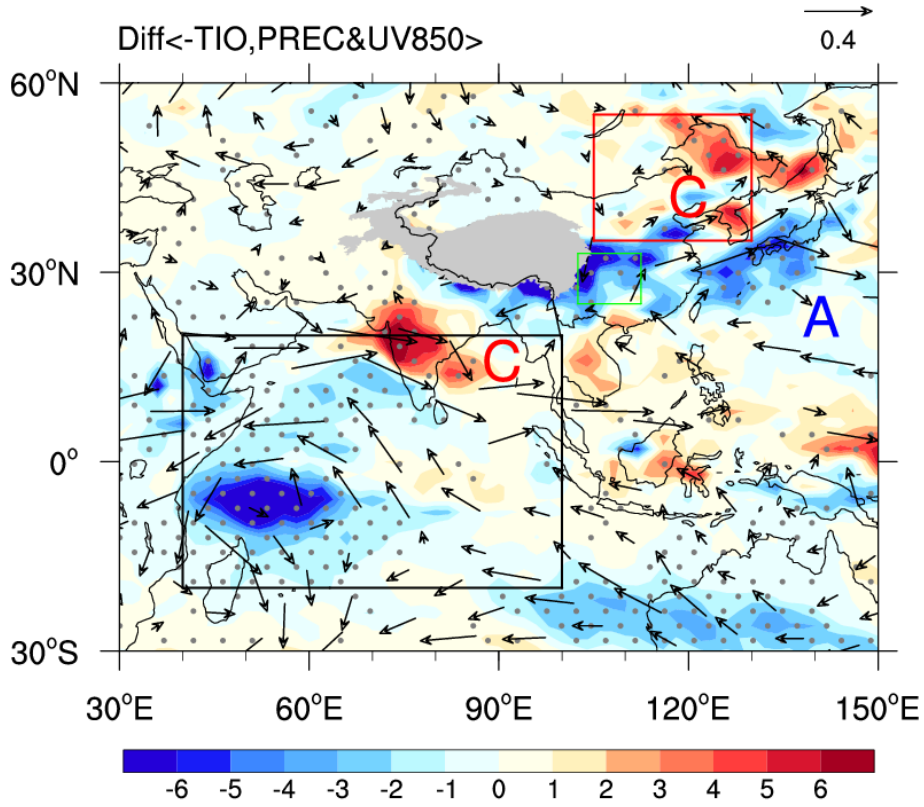
885

886

887

888

Figure 9. Partial regression of the JJA-mean (a) Z400 (shading; m) and UV400 (vectors; m s^{-1}), (b) Z850 (shading; m) and UV850 (vectors; m s^{-1}), (c) $\langle \text{WVT} \rangle$ (vectors; $\text{kg m}^{-1} \text{s}^{-1}$) and $\langle \text{WVT}_{\text{div}} \rangle$ (shading; $10^{-5} \text{ kg m}^{-2} \text{s}^{-1}$), and precipitation (mm month^{-1}) anomalies onto the concurrent negative I_{IOBM} with the IPO signal removed during the period 1901–2014. All variables are detrended and 11-year low-pass filtered. Areas with significant values of Z400, Z850, and $\langle \text{WVT}_{\text{div}} \rangle$ that exceed the 95% confidence level are stippled, respectively. Only vectors that are significant at the 95% confidence level are shown. The I_{IOBM} /IPO index is calculated based on the ERSSTv5 dataset; the precipitation is derived from the CRU TS3.26 precipitation data; whilst other variables are from the 20CRv2c datasets.



889

890

891

892

893

894

895

896

897

898

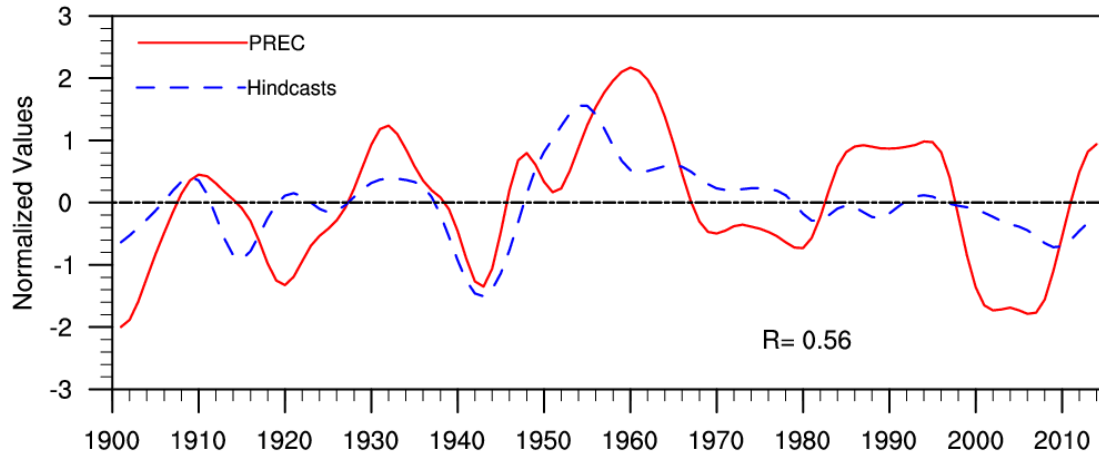
899

900

901

902

Figure 10. Simulated composite differences of JJA-mean UV850 (vectors; m s^{-1}) and precipitation (shading; mm month^{-1}) between cold and warm SST years over the broader TIO domain in CESM1_IOPES (15°S – 15°N , 40° – 174°E ; purple box in **Fig. S4**). The warm and cold TIO SST years are selected based on the ± 0.5 standard deviations of the simulated time-evolving SSTAs during 1920–2005, as shown in **Fig. S3** (red line). All variables are detrended and 11-year low-pass filtered. Areas with significant values of precipitation that exceed the 95% confidence level are stippled. Only vectors that are significant at the 95% confidence level are shown. The simulated anomalies of UV850 and precipitation are calculated based on the difference between the CESM1_IOPES ensemble mean and the CESM1_LENS ensemble mean (former minus latter), highlighting the internally driven impacts of TIO SSTAs.



903

904

Figure 11. Normalized time series of the JJA-mean I_{EAMBZP} (red line) and associated leave-one-out cross-validated hindcast estimates (blue line) for 1901–2014, with the number denoting the TCC between the corresponding time series.

905

906

907

908

909

910

911

912

913

914

915

916

917

918

919

920

921

922

923

924

925

926

927

928

929

930

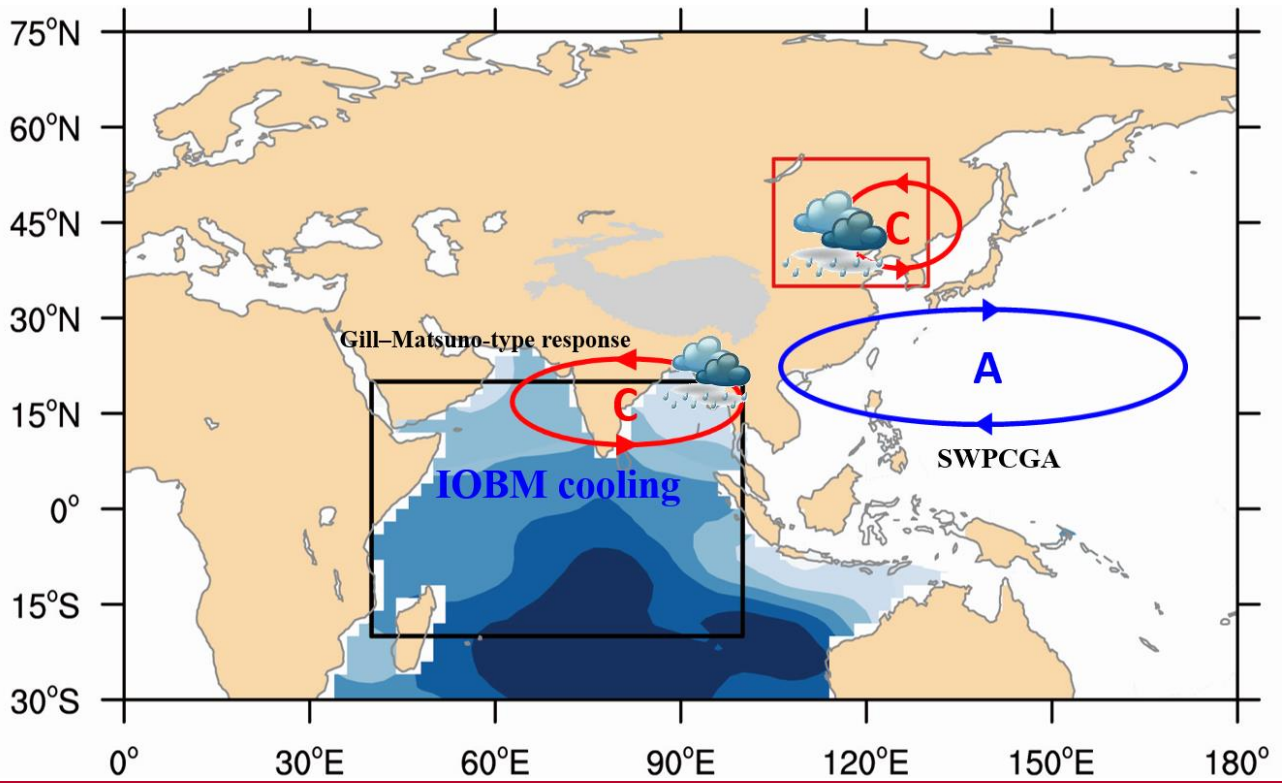
931

932

933

934

935



936
937
938
939
940
941
942
943

Figure 12. Schematic diagram showing how IOBM-related SST anomaly pattern drives the summer EAMBZ precipitation fluctuations at interdecadal timescales. Blue shading illustrates the IOBM cooling. Letter A (C) indicates the center of the anticyclonic (cyclonic) gyre anomaly.